INTERNATIONAL ATOMIC ENERGY AGENCY
UNITED NATIONS EDUCATIONAL, SCIENTIFIC AND CULTURAL ORGANIZATION
INTERNATIONAL CENTRE FOR THEORETICAL PHYSICS
I.C.T.P., P.O. BOX 586, 34100 TRIESTE, ITALY. CABLE CENTRATOM TRIESTE

SMR.703 - 5

WORKING PARTY ON
MECHANICAL PROPERTIES OF INTERFACES

23 AUGUST - 3 SEPTEMBER 1993

"Semiconductor Multilayers"

"Principles and Concepts of Strained-Layer Epitaxy" (Part I)

R. HULL
AT&T Bell Laboratories
600 Mountain Avenue
Murray Hill, NJ 07974-0636
U.S.A.

CHAPTER 1

Principles and Concepts of Strained-Layer Epitaxy

R. Hull and J. C. Bean

AT&T BELL LABORATORIES
MURRAY HILL, NEW JERSEY

I. Introduction

Atomic-scale growth control of artificially modulated structures by advanced crystal-growth techniques such as molecular-beam epitaxy (MBE) and metal–organic chemical vapor deposition (MOCVD) has in the last decade

extended the frontiers of materials science, physics, and semiconductor device performance. Historically, the initial focus has been on the growth of material combinations with essentially the same crystal lattice parameter and structure, e.g., $Al_xGa_{1-x}/GaAs$. Although the growth of ultrahigh electrical and structural quality material in these and similar systems has required both perseverance and inspiration, the fundamental physical constraints on successfully defining the epitaxial structure (i.e., point and line defect free, with planar surface morphology) are greatly eased when the equilibrium structure of the grown layers corresponds closely to that of the substrate.

Interest in extending the range of possible material combinations has, however, encouraged experimentation in lattice-mismatched epitaxial structures. In addition to the problems encountered (and to a large extent, solved) in lattice-matched epitaxy, the primary extra complication introduced by this extra degree of freedom is the introduction of extended defects that attempt to relieve elastic strain in the structure. Understanding and control of these defects appears to be the principal challenge faced in strained-layer epitaxy, and progress to date will be discussed in detail later in this chapter. Other phenomena present in lattice-matched epitaxy, e.g., surface diffusion and clustering phenomena, may be more significant in mismatched-epitaxy, due to the likelihood of a greater chemical dissimilarity between materials in the structure. Indeed, we shall aim to show in this chapter that each and every stage in the heteroepitaxial growth process, from substrate preparation to post-growth processing, is of critical importance in determining the final structure.

The field of strained-layer epitaxial growth is very much in its formative stages and is continually evolving. Care will be taken in this chapter to attemt to differentiate among those problems that appear presently to be understood, those in which an understanding is being developed, and those that to date remain intractable. The following fundamental stages of the heteroepitaxial growth process should be considered:

(i) Construction of a suitable growth chamber;

(ii) Preparation of the substrate surface;

(iii) Possible growth of a homoepitaxial buffer layer onto the as-cleaned substrate surface;

(iv) Nucleation of the heteroepitaxial layer: clustering or layer-by-layer growth;

(v) Introduction of extended defects (if critical-layer dimensions are exceeded) to relax the elastic strain introduced by lattice mismatch;

(vi) Evolution of the growth surface, i.e., coalescence of individual nuclei, or possibly roughening of a planar surface. Note that this stage could occur before or after step (v); and

(vii) Redistribution of defect populations within the epitaxial layer, such as by defect "filtering" via incorporation of strained-layer superlattices or termination of a dislocation at the edge of a structure.

Each of these processes will be discussed in succeeding sections of this chapter. Our aim will not be to review exhaustively all work done in the field (specific materials systems are reviewed in other chapters of this volume), but rather to outline the fundamental physical processes involved in strained-layer epitaxy and to illustrate them with specific examples.

II. Growth Techniques

A. Introduction

The fundamental tool of lattice-mismatched epitaxy is the crystal-growth chamber. The major requirements of a growth chamber for high-quality epitaxial growth include: a noncontaminating (ultrahigh vacuum or inert) environment; source purity; a source-substrate geometry that allows deposition uniformity; uniform substrate heating cooling; absence of particulates and undesired impurity atoms; sufficient analytical techniques to allow in situ monitoring of growth quality and control of layer composition and thickness. In a research environment, throughput of wafers is less critical, therefore ultrahigh vacuum (UHV) techniques, particularly solid-evaporation-source MBE, are acceptable. MBE has two relevant advantages: (1) exceedingly good control of layer dimensions and composition; (2) growth at minimal temperatures (generally well below those required for significant bulk diffusion but not necessarily surface diffusion). Low-temperature growth is an absolute requirement if one is to attempt metastable strained-layer epitaxy (as in the germanium silicide system).

The following sections give a brief overview of the crystal growth techniques being used for strained-layer growth including molecular-beam epitaxy, atomic-layer epitaxy, gas-source molecular beam epitaxy and chemical vapor deposition (CVD). However, in subsequent sections, discussion will tend to focus on MBE. This is justified by the current dominance of MBE in strained-layer epitaxy and by the fact that, with MBE, it is particularly straightforward to define the role of substrate preparation, impurity effects, and nucleation. Nevertheless, the reader should bear in mind that these issues and discussions are generic to all crystal growth techniques.

B. Molecular-Beam Epitaxy and Atomic-Layer Epitaxy

Some important principles of the MBE growth technique are illustrated in Figs. 1a and 1b. The essential requirement for a MBE growth chamber is that

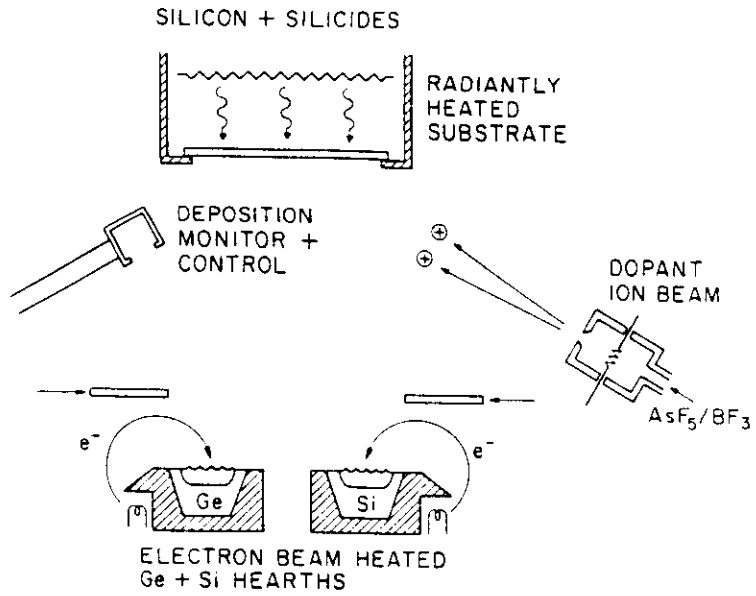

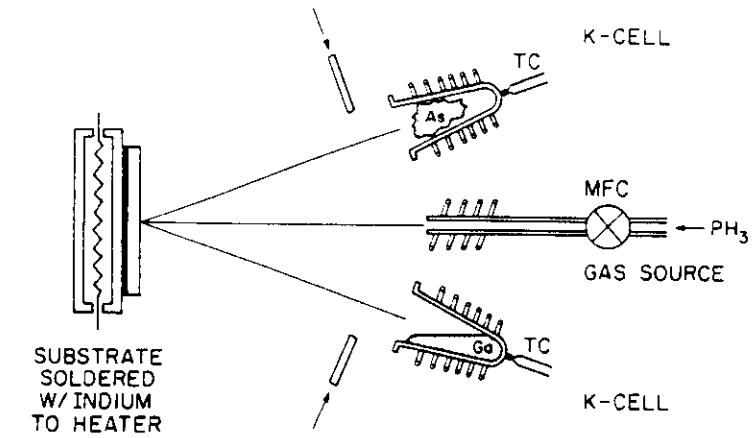

FIG. 1. Schematic diagram of a molecular-beam epitaxy growth chamber (a) for column-IV deposition, (b) for III–V deposition.

growth take place at a sufficiently high vacuum so that arrival and sticking of impurity atoms from the ambient occur at a negligible rate. This is particularly important in the growth of strained-layer heteroepitaxy. On growing surfaces, impurities can massively perturb growth by providing heterogeneous cluster or defect nucleation sites. Within the crystal, impurities may precipitate to form nucleation sites for strain-relieving dislocations.

To first order, impurity gas impingement varies inversely with partial pressure with a pressure of 10^{-6} torr producing a flux of 1 atomic monolayer per second. Thus, a total chamber pressure of 10^{-10} torr corresponds to an arrival rate of $\sim 10^{-4}$ atoms or molecules sec^{-1} cm^{-2} on the growth surface. For typical MBE growth rates of ~ 1 monolayer sec^{-1}, this relatively low arrival rate would still produce an unacceptably high impurity concentration in the growing epilayer, were the sticking coefficient for the impurities unity.

Fortunately, at the elevated temperatures (of the order of 700–1200 K) generally employed during substrate cleaning and epilayer growth, sticking coefficients for most UHV constituents are many orders of magnitude less than one, permitting high purity growth. However, there are exceptions, and these exceptions strongly affect the design of the MBE growth chamber. In particular, growing AlAs and AlGaAs alloys have an extremely strong affinity for oxygen derived from the strength of the oxygen–aluminium chemical bond. Oxygen can affect layer morphology and electronic carrier transport. In a leak-free MBE system, this oxygen comes from decomposition of ambient water vapor held over from earlier venting of the vacuum chamber. This can be largely eliminated by the addition of extensive internal shrouds filled with liquid nitrogen on which the water is trapped. With the advent of plumbed-in liquid-nitrogen supply systems, these shrouds are frequently cooled not only during growth but continuously, over months of operation.

The strength of the carbon–silicon bond poses a similar problem in MBE of silicon and silicon alloys. Although carbon is relatively soluble in silicon, its presence at a growing crystal surface can lead to the formation of silicon carbide nuclei. These nuclei are extremely stable and, given their hexagonal crystal structure, they provide ready sites for defect nucleation in the cubic silicon lattice. Carbon can come from several sources. It is present in all but the most carefully controlled chemical cleaning solutions. Even if such control is maintained, an atomically clean surface will immediately react with carbon in ambient air. Ex situ cleaning is therefore generally terminated with the formation of a comparably inert chemical oxide that can be readily reduced and desorbed by heating in vacuum. While such surfaces are adequate for basic studies of silicon homoepitaxy, residual carbon can still adversely affect heteroepitaxial nucleation and strained-layer relief, as detailed later.

Carbon may also come from the decomposition of oils used in certain vacuum pumps. In the last decade or so, such pumps had been largely

eliminated in favor of oil-free ion pumps and closed-cycle He cryogenic condensation pumps. Recently, however, manufacturability issues have stimulated renewed interest in gas-source MBE or MBE/CVD hybrid vacuum technologies. Ion pumps cannot handle significant gas loads, and the accumulation of typical gas-source chemicals within cryogenic pumps poses both toxic hazards and the possibility of ignition and/or explosion. Gas-source systems must therefore use nonaccumulating pumps such as diffusion pumps or turbo-molecular pumps. Carbon contamination from such pumps proved to be the bane of early attempts at silicon MBE (Joyce, 1974). The challenge is thus to develop hydrocarbon trapping techniques and chemically resistant oil-free fore-pumps. Whereas this might appear to be a problem unique to silicon MBE, the handling of fore-pump oils contaminated with III–V toxic materials is already a significant safety concern. At least one organization is already recommending the elimination of conventional oil fore-pumps on all gas-source systems.

Ironically, the reduction of oxygen and carbon contamination in solid-source MBE systems has introduced another defect-producing mechanism: particulates. In a solid-source MBE system (or a hot-wall CVD-like system), material will deposit in areas other than the targeted substrate. If vacuum is maintained for long periods, the buildup of material will produce strains leading to fracture and the release of very fine particulates. (Gross flaking may also occur, but it poses less of a problem.) Under the influence of applied electric fields or even typical MBE vapor fluxes, these particulates can actually be propelled upward onto a growing epitaxial surface (Matteson and Bowling, 1988).

Uncontrolled, these particulates can produce defect densities of 100–1000 per square centimeter (Bellevance, 1988). There are two emerging strategies to control this problem. This first is to tightly columnate the deposition fluxes to the substrate surface alone. The columnators are then replaced or cleaned of accumulated deposits at each vacuum break. The second approach is to grossly reduce thermal cycling within the MBE chamber, thereby maximizing deposit adhesion. In AlGaAs systems, this is accomplished by continuous cooling of liquid-nitrogen shrouds. In silicon-based MBE systems, the newest generation of equipment goes one step further. Because oxygen does not bond strongly to heated silicon, water vapor is not as critical a concern. Liquid-nitrogen shrouding is thus being removed from the growth area in favor of water cooling of either shrouds or chamber walls (e.g., Parker and Whall, 1988).

Assuming one can provide a suitably clean environment for molecular-beam epitaxy, the next problem is that of controlling layer composition. In an alloy system, such as Ge_xSi_{1-x}, significant errors may be tolerable. Growth of compounds, e.g. GaAs, however, requires control of stoichiometry to levels

better than one part per million. If such control is not maintained, second-phase inclusions will form and crystal growth will be massively disrupted. Figures 1a and 1b illustrate typical schemes for the growth of III-V and column-IV materials, respectively. Neither temperature-controlled Knudsen cells, mass-flows-controlled gas sources, nor sensor-controlled electron guns offer the requisite part-per-million regulation.

MBE thus depends on one of two mechanisms to maintain stoichiometry. For common III-V semiconductors, it was found that although the column-V species will bind tightly to a freshly deposited column-III layer, it will not bond well to another column-V layer. In terms of GaAs, this is to say that As will bind to Ga but tends to re-evaporate from another layer of As. Stoichiometry is thus maintained if one provides an excess flux of the column-V species. The crystal then adsorbs only the species it requires.

Atomic-layer epitaxy (ALE) simply takes this process one step further: For example, in growth of certain II-VI semiconductors, the complementary process is also active, and whereas column-II materials will bind to column VI, neither will bind to itself (at appropriate growth temperatures). Growth rate is then independent of the incoming flux and depends only on the number of times the substrate is exposed to alternate pulses of column-II and VI atoms (as each pulse produces a single, self-limiting atomic layer of deposition). This self-balancing process is essentially the same as that active in liquid-phase epitaxy or chemical vapor deposition.

The second self-balancing mechanism is operative in MBE growth of compounds such as $CoSi_2$ on Si. Neither Co nor Si will re-evaporate, but excess Co will readily diffuse through a thin $CoSi_2$ layer to react at the silicon substrate. In essence, stoichiometry is achieved by simultaneous vapor-phase crystal growth at the surface and solid-phase growth at the substrate. Excess metal fluxes may thus be used in thin layers, but as the epilayer thickness increases, diffusive transport of Co through the epilayer becomes increasingly difficult, and growth will ultimately break down.

C. Gas-Source Molecular-Beam Epitaxy

For the purposes of this chapter, gas-source MBE (GSMBE) can be considered a simple derivative of the solid-source process. Gas sources address three weaknesses of conventional MBE. First, Knudsen evaporation sources have a finite capacity (of the order of 50–100 cc) and may be depleted within as little as a month. This is particularly true for the column-V species, where excess fluxes must be maintained in order to assure stoichiometric growth of a III–V compound. Further, before a cell is fully depleted, there will be serious shifts in evaporation rates due to the reduction of charge size. To compensate for this, frequent, sacrificial calibration runs must be made, and for very critical structures, the shift of calibration within a single run may

become unacceptable. The use of external, easily replaceable, gas cylinders eliminates this problem. Fluxes are continuously calibrated and regulated by mass-flow controllers or temperature baths. Moreover, the elimination of vacuum breaks not only increases chamber up-time but can result in a significant overall reduction of vacuum impurity levels.

Gas sources have a second advantage in that they overcome difficulties in handling pyrophoric species such as white phosphorus. Phosphine, although highly toxic, is not spontaneously flammable and with proper handling will not accumulate within the MBE system. This has opened the door to the highly successful growth of GaInAsP species by MBE.

Finally, with certain chemistries and growth temperatures, the species from gas sources may decompose at the heated substrate surface alone. There will be little or no wall deposition, and the elimination of such accumulations will largely eliminate particulate contamination due to flaking. Although not currently recognized as an issue in III-V MBE, it has been shown that solid-source wall deposits can limit silicon MBE materials to defect densities of above 100–1000/cm^2, as discussed earlier.

D. Chemical Vapor Deposition

Turning history around a bit, CVD can be viewed as a high-pressure variant of gas-source MBE (GSMBE). The chemistries are fundamentally similar; the differences depend primarily on what is done with the gaseous species. In CVD, gaseous species are delivered to the substrate wafer in their original form, that is, as column-V hydrides or column-III organics. In GSMBE, the hydride is often thermally "cracked" into a subhydride or pure column-V species by passing through a heated nozzle (often including a catalyzing metal). For the purposes of this chapter, the major possible advantage of this cracking process is that it can permit growth of epitaxy at lower substrate temperatures. This could be important if one is attempting to maintain strained-layer epitaxy to thicknesses above equilibrium limits. The reduction of temperature would then inhibit nucleation and growth of defects and thus reduce the relaxation of strain. However, to date, such metastable growth has only been well documented in the GeSi system. Thus, for the bulk of III-V growth, the absence of precracking places CVD at no significant disadvantage, and enhancements in wafer size and sample preparation may actually make it more desirable than MBE for the bulk of III-V growth systems.

III. Importance of the Substrate Surface in Heteroepitaxial Growth

The initial stage of the deposition process is to obtain a suitable surface on which to initiate growth. The primary concern is to obtain a surface that is atomically clean, i.e., stripped of its native oxide and free of any other surface

or near-surface contaminants. To prevent reoxidation or contamination of the cleaned surface, at least the final stages of the cleaning process are usually done in situ under UHV conditions.

In general, the requirements for cleaning elemental column-IV substrates are more stringent than those for cleaning of III-V-compound semiconductor substrates. This is driven both by technological requirements and by the fact that native oxides desorb at significantly lower temperatures for the latter class of materials. By current standards, an adequate GaAs substrate can be prepared by ex situ wafer degreasing, followed by in situ oxide desorption at ~ 600°C and growth of a homoepitaxial buffer layer. To produce state-of-the-art Si epitaxy, much more ingenuity and care are required. Tendencies toward islanded growth also make silicon substrate preparation a major issue in strained-layer growth of disparate materials such as GaAs on Si.

Conventional silicon substrate cleaning techniques fall into three general classes: (i) ex situ chemical cleaning followed by growth of a relatively volatile surface $SiO_x (x \sim 1)$ layer, followed by in situ desorption of the volatile oxide, this occuring at much lower temperatures than for the native SiO_2 oxide; (ii) in situ removal of the surface and near-surface region by sputtering with inert (generally argon) ions, followed by a thermal anneal to remove sputtering damage; (iii) in situ back-etching of the substrate under chlorine gas to remove several hundred angstroms of material. Only the later back-etching technique has demonstrated quality adequate for commercial production of complex integrated circuits. Unfortunately, its use is restricted to halogen CVD growth, and virtually all the work in this book is based on the first two approaches.

In the first class of cleaning techniques, the major requirements are first to chemically strip the Si-substrate surface in a manner that does not leave any detectable contaminants, especially carbon or metallic species, second, to produce a volatile oxide layer of uniform stoichiometry and thickness, and third, to successfully desorb the volatile oxide in situ in the growth chamber. None of these requirements are easy to satisfy. A variety of chemical cleaning techniques have been developed to satisfy the first two requirements above, e.g., the Henderson (1972) and Shiraki–Ishizaka (Ishizaka *et al.*, 1983) cleans. The latter treatment is most widely used and consists of repeated oxidation and stripping of the surface in nitric and hydrofluoric acids, respectively, followed by growth of an approximately 10-Å-thick SiO layer in a hydrogen peroxide–hydrochloric acid mixture. In the original reference, it was suggested that desorption temperatures as low as 750°C would be sufficient to produce an oxygen-free surface; it has been our experience and that of others (e.g., Xie *et al.*, 1986) that somewhat higher temperatures ($> \sim 900$°C) are required to produce truly clean surfaces using this technique. This is illustrated by secondary ion mass spectroscopy (SIMS) data showing the residual surface contamination following Shiraki oxide desorption at various temperatures in Fig. 2.

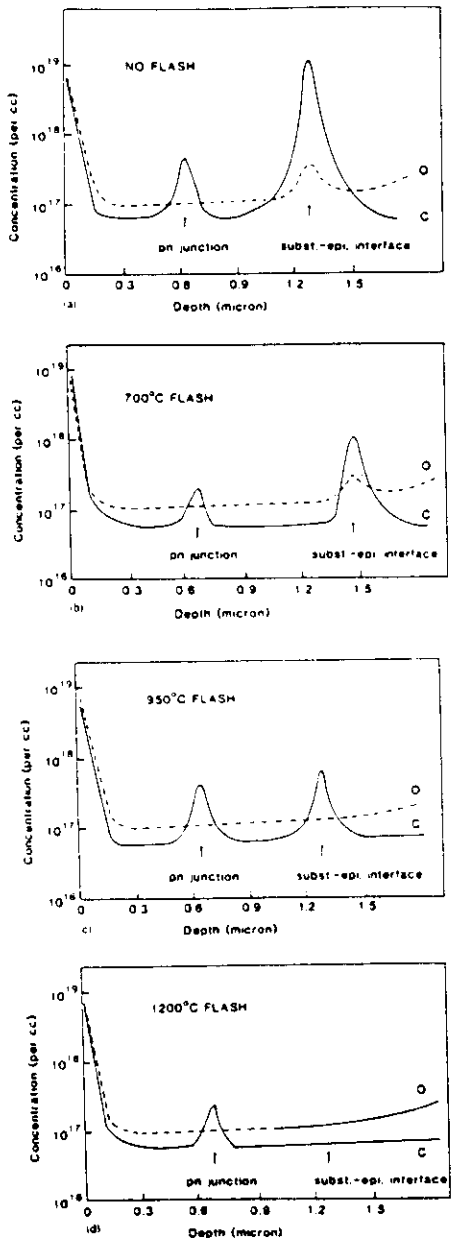

FIG. 2. Secondary ion mass spectroscopy of residual O and C surface contamination following Shiraki cleaning of Si(100) wafers at various SiO desorption temperatures (from Xie *et al.*, 1986).

A number of variants of the basic Henderson and Shiraki methods have been developed. Oxide desorption has been shown to be more effective when a Si flux impinges upon the surface (Tabe *et al.*, 1981; Hardeman *et al.*, 1985), presumably because pockets of O-rich SiO_x can be converted to the correct monoxide stoichiometry. Another variant involves ozone cleaning under ultraviolet irradiation between the volatile oxide growth and desorption stages (Tabe, 1984); this technique has been shown to be extremely effective at reducing surface organic contaminants, reducing homoepitaxial defect densities by ~ 2 orders of magnitude on Si(100) and (111) surfaces for desorption temperatures of 800–900°C.

The second major class of cleaning techniques consists of in situ sputtering with inert gas ions to remove the near-surface region. In our laboratory, Si surfaces are cleaned using $\sim Ar^+$ ions accelerated to 0.2 keV, with the substrate held at room temperature. Approximately 100 Å of material is removed, leaving a clean but disordered surface. The substrate is then annealed at 750°C for five to fifteen minutes. The amorphous surface layer reorders by solid-phase epitaxy as the sample passes through 500–600°C, and residual point defects are annealed out at 750°C. Defect densities in homoepitaxial layers grown upon these cleaned surfaces are of the order of 10^2–10^3 cm^{-2}, comparable to or better than Shiraki-type cleaning techniques at 800°C.

A recently developed cleaning technique (Grunthaner *et al.*, 1988) offers promise of clean Si surfaces at far lower temperatures. This process involves ex situ removal of a thin 10 Å chemical oxide by spinning in a N_2 dry box loadlocked to the MBE chamber, while rinsing/etching first in pure ethanol (added dropwise), then in 1:10 HF:ethanol, and finally in pure ethanol. This technique produces an atomically clean (to a level at least comparable to standard in situ volatile oxide desorption at temperatures of ~ 800°C) hydrogen-passivated 1×1 surface after heating to 150°C. Conversion to a 7×7 reconstruction on a (111) surface occurs at temperatures of ~ 500°C.

Although further improvements in Si cleaning techniques are both preferable and possible, it appears that careful control of these processes can produce Si surfaces that are sufficiently clean to allow high-quality heteroepitaxial growth upon them. An area that has hitherto received little attention, however, is the effect of the substrate cleaning on surface morphology and the resultant heteronucleation stage. For growth on Si substrates, we have observed that both major classes of cleaning techniques can affect the surface morphology and influence the initial stages of heteroepitaxial growth.

In Fig. 3, we show high-resolution cross-sectional transmission electron microscope (TEM) images of the early nucleation stages of GaAs grown on a Si substrate cleaned by the Ishizaka process (for exact details, see Koch *et al.*, 1987). The substrate orientation is with the surface normal 4 degrees from

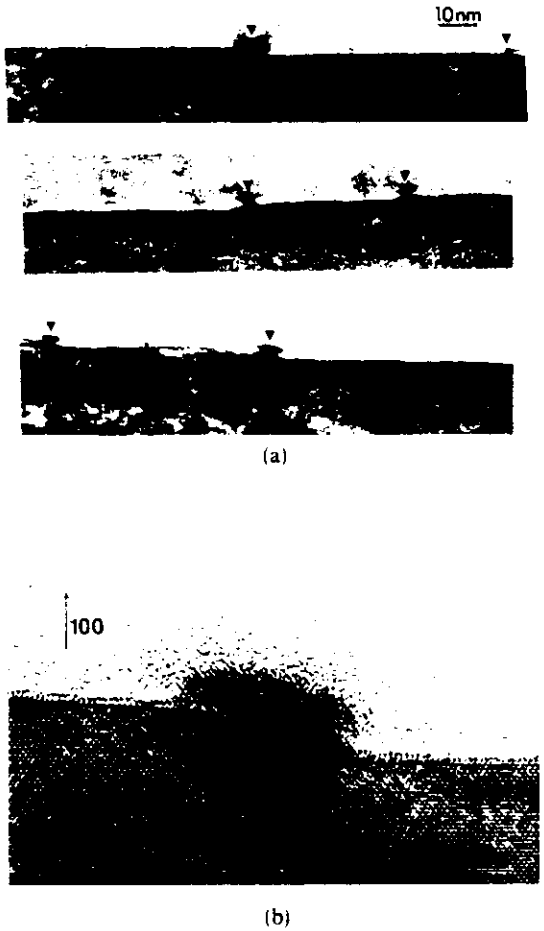

FIG. 3. (a) Cross-sectional TEM images of GaAs nucleation onto a vicinal (4 degrees toward ⟨011⟩)Si(100) wafer following SiO desorption at 880°C for 20 minutes. Note nucleation of GaAs on surface facets (arrowed) (from Hull *et al.*, 1987b); (b) lattice structure image of one facet (from Hull *et al.*, 1987a, b).

[100], the direction of the misorientation being towards an in-plane ⟨011⟩ azimuth. Growth of GaAs on such misoriented wafers historically believed to produce a uniform array of (200) steps on the Si surface, which prevents the formation of antiphase boundaries at the GaAs–Si interface (e.g., Kroemer, 1986).

From the images of Fig. 3, we note, however, that the Si substrate surface does not consist of a regular array of (200) steps and (100) terrace, but rather

displays a distribution of "step groups" approximating low-angle facets many monolayers high. Note that nucleation of GaAs islands (arrowed) is associated with these facets. The effect of this facet–nucleation correlation is strongly demonstrated in Fig. 4, which is a "plan-view" TEM image where the electron beam is approximately (depending on the exact electron diffraction conditions used) perpendicular to the Si surface. The GaAs nuclei show as long strings of material nucleating along the [011] direction of the crystal, which equates to the direction of surface steps induced by the deliberate substrate misorientation. By comparing measured facet heights with the measured distances between "strings" of GaAs nuclei (Hull *et al.*, 1987a,b), we have been able to show statistically that the GaAs nucleation density is controlled by the substrate surface facet distribution.

We have ascertained by TEM that the interface between the as-grown volatile oxide and substrate surface (i.e., before the oxide desorption stage) is not similarly facetted. Thus the surface facetting appears to occur during the oxide desorption stage. In situ reflection high-energy electron diffraction (RHEED) measurements show that the initial surface structure of the misoriented Si(100) surface during the early stages of the oxide desorption process is a combination of the two orthogonal $(2 \times 1) + (1 \times 2)$ reconstructions possible on the (100) surface. The presence of these two domains indicates the existence of single monolayer (400) steps on the Si surface. As oxide desorption progresses, the RHEED pattern generally evolves into that expected from a single 2×1 surface domain, indicating reconstruction of pairs of (400) into (200) steps (see, e.g., Kaplan, 1980; Kroemer, 1986). Note that the efficiency of this process depends on the magnitude of the substrate misorientation toward [011], being most effective for tilts of 2–4 degrees (Koch *et al.*, 1987; Griffith *et al.*, 1988; Wierenga *et al.*, 1987). This is demonstrated beautifully by the scanning tunneling microscope images of

FIG. 4. Plan-view TEM image of the structure imaged in cross-section in Fig. 3. Note anisotropic nucleation of GaAs along ⟨011⟩ facets (Hull *et al.*, 1987a,b).

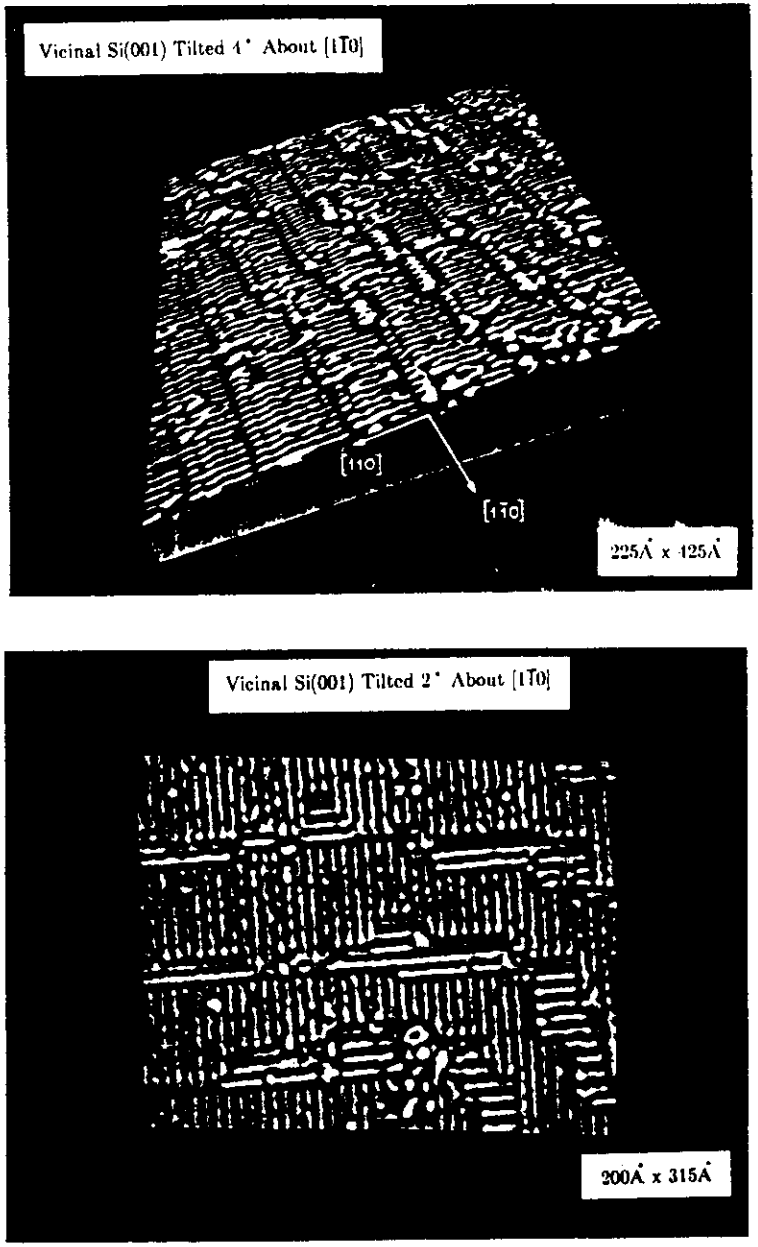

FIG. 5. Scanning tunneling microscope image of (a) a 4-degree and (b) a 2-degree misoriented (toward an [011] azimuth) silicon (100) surface, cleaned by Ar^+ annealing and sputtering. A higher proportion of double monolayer steps exists on the higher misorientation surface. (From Griffith, G. P. Kochanski, J. A. Kubby and P. E. Wierenga, J. Vac. Sci. Tech. A1, 1989).

Fig. 5, which demonstrate the difference in step structure for "low" and "high" substrate misorientations.

The oxide desorption temperature used in these experiments, ~900°C, is well below the expected roughening temperature on Si(100) surfaces. Measurements of the degree of surface facet height as a function of oxide desorption time (Hull *et al.*, 1987c) shows increasing facetting with longer time at the desorption temperature. A preliminary model for this facetting mechanism is shown in Fig. 6. Local nonstoichiometries (oxide rich, probably SiO_2) in the Shiraki oxide require excess Si to achieve the correct SiO composition for low temperature desorption. In the absence of an impinging Si flux, this excess Si may arrive only from the substrate. The easiest way to provide the required Si flux is via flow of surface steps (produced by the substrate misorientation) towards the O-rich region. In this manner, a facet is produced at this location. A similar mechanism of Si surface diffusion has been identified during decomposition of SiO_2 on Si(100) via reduction to SiO (Tromp *et al.*, 1985; Rubloff *et al.*, 1986). Motion of surface steps could also be impeded by surface impurities such as carbon, again producing step "groups." Nucleation studies of GaAs on vicinal Si(100) using UV-ozone substrate cleaning have demonstrated a much lower degree of facetting and significantly more isotropic nucleation of GaAs/Si (Biegelsen *et al.*, 1988), suggesting a more uniform Shiraki oxide and/or lower surface contamination levels by this technique. It has also been suggested that As adsorption onto a vicinal Si(100) surface can itself produce a facetting transition as the sample is cooled through a temperature of ~800°C (Ohno and Williams, 1989).

The above results indicate that the heteronucleation process can be strongly influenced by the substrate cleaning technique and may in fact be controllable by suitable choice of a substrate surface "template." We note also that ion sputter cleaning of Si substrates may also influence surface structure and subsequent heteronucleation (Hull *et al.*, 1987c). Since cleaning of III-V compound semiconductor substrates is generally easier and more standardized, we are not aware of any similar reports in which the surface cleaning technique has been correlated to the nucleation mode in III-V epitaxy. Certainly, in the limit where the cleaning technique significantly affects surface stoichiometry and morphology, however, such effects would be very likely. These are most likely to arise where integrated growth of different

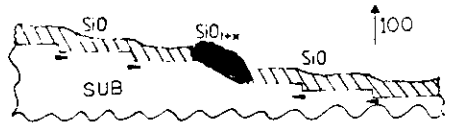

FIG. 6. Schematic illustration of possible model for surface facetting on Shiraki-cleaned vicinal Si(100) surfaces. (From Hull *et al.* 1987c. Paper originally presented at the Fall 1987 meeting of the Electrochemical Society held in Honolulu, Hawaii).

semiconductor "families" practically prevents growth of a homoepitaxial b uffer layer onto the original cleaned surface. In the example given earlier, GaAs is usually grown on Si substrates in modified III-V MBE chambers or in MOCVD chambers without a silane source. Thus, GaAs is deposited directly onto the as-cleaned Si surface without intervention of a Si buffer layer. Such a buffer layer, if present, might be expected to modify the as-cleaned surface morphology. In compound semiconductor growth, before deposition of, say, a III-V heterostructure on a GaAs substrate (e.g., AlGaAs/GaAs or InGaAs/GaAs), growth of a homoepitaxial buffer layer on the as-cleaned substrate is standard. This might be expected to effectively bury any as-cleaned surface nonstoichiometries or other anomalies. In "mixed" deposition, such as deposition of II-VI materials onto a III-V substrate without intervention of a homoepitaxial buffer layer, the effect of the surface clean is more likely to be noticeable. An example of this is the fascinating phenomenon of "double positioning" observed for growth of CdTe/GaAs (Kolodziejski *et al.*, 1986; Faurie *et al.*, 1986a; Ponce *et al.*, 1987), where CdTe deposited directly onto an as-cleaned GaAs substrate is observed to grow in two separate epitaxial orientations (100_{GaAs} parallel to 100_{CdTe} and 100_{GaAs} parallel to 111_{CdTe}), as shown in Fig. 7. This effect has been correlated to the extent of the presence of residual oxide on the cleaned GaAs surface. Development of linked "double-chamber" systems, with growth of III-V materials in one chamber and II-VI materials in the other will help overcome such difficulties. Note that it has also recently been reported (Reno *et al.*, 1988) that deliberately induced substrate misorientation can improve the structural quality of growth of (111) CdTe on (100) GaAs, and that for growth of $Cd_{1-x}Zn_xTe$/GaAs(100), the epitaxial orientational relationship between substrate and epilayer depends upon the composition x (Faurie *et al.*, 1986b).

IV. Nucleation and Growth Modes

A critical factor in the practical applicability of strained-layer heteroepitaxial structures is the thickness uniformity of the grown layers. Three general heteroepitaxial growth modes have been observed, as illustrated in Fig. 8: (a) layer-by-layer or two-dimensional growth (Frank–Van der Merwe mode) of the epilayer; (b) clustered or three-dimensional growth (Vollmer–Weber mode); and (c) a hybrid growth mode known as Stranski–Krastanow (Stranski and Krastanow, 1939; Bauer and Poppa, 1972; Fisanick *et al.*, 1988), in which the growth mode is initially layer-by-layer for a few monolayers and subsequently clusters. Unfortunately, the general growth mode of an epitaxial layer on a chemically dissimilar substrate consists of nucleation of clusters of the deposited material, as may be seen from the force balance equation for the

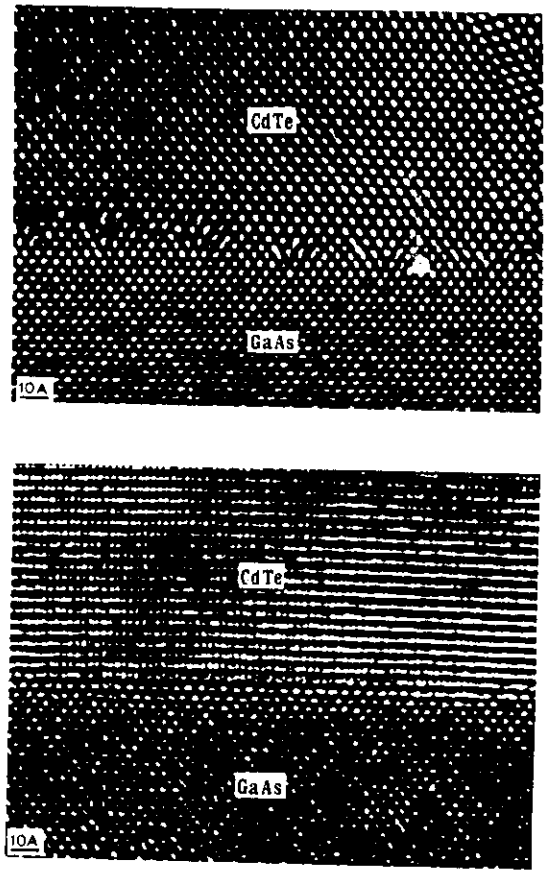

FIG. 7. Cross-sectional electron microscope images of double positioning of CdTe GaAs(100): (a) [100] CdTe parallel to [100] GaAs; (b) [111] CdTe parallel to [100] GaAs (from Kolodziejski, *et al.*, 1986. Micrographs supplied by N. Otsuka).

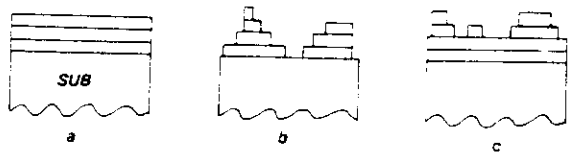

FIG. 8. Schematic illustration of the three primary heteronucleation modes: (a) layer-by-layer (Frank–Van der Merwe); (b) clustered (Vollmer–Weber) and (c) Stranski–Krastanow.

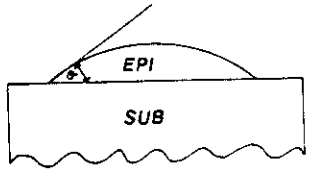

FIG. 9. Schematic illustration of the liquid-drop model for predictiong equilibrium cluster contact angles.

liquid-drop model of a nucleus,

$$\sigma_{sv} = \sigma_{es} + \sigma_{ev}\cos\theta, \tag{1}$$

where σ_{sv} is the energy per unit area of the substrate–vapor (for MBE, the substrate–vacuum) interface, σ_{ev} is the energy per unit area of the epilayer–vapor interface, σ_{es} is the energy per unit area of the substrate–epilayer interface, and θ is the contact angle between epilayer and substrate, as defined in Fig. 9. Unless there is a fortuitous combination of surface and interface energies, the above equation will only be identically true for layer-by-layer growth ($\theta = 0$) for homoepitaxy, where $\sigma_{sv} = \sigma_{ev}$ and $\sigma_{es} = 0$ or for the case where $(\sigma_{sv} - \sigma_{es})/\sigma_{ev} > 1$, i.e., where the substrate surface energy is high relative to the interface and epilayer surface energies. Thus, the general heteroepitaxial nucleation mode will be clustered, or three-dimensional, growth. Note that the diquid drop model does not take into account the effect of lattice-mismatch rain.

Equation (1), however, assumes that the structure can reach its equilibrium state and is thus effectively assuming infinite surface diffusion lengths to form the necessary clusters. In epitaxial growth, surface diffusion lengths may be controlled primarily by (i) substrate temperature, and (ii) by deposition rate. Lower substrate temperatures will mean lower, or perhaps even negligible, diffusion lengths and therefore promote layer-by-layer or two-dimensional growth, assuming uniform arrival of atomic/molecular flux at the growth surface. If the temperature is too low, however, this will be at the expense of crystalline perfection. In Fig. 10, we show the tendency for two-dimensional (2D) versus three-dimensional (3D) growth as functions of alloy composition and substrate temperature in the Ge_xSi_{1-x} Si(100) system (Bean *et al.*, 1984). Note that the tendency for 3D growth is reduced both by lowering the substrate temperature and by decreasing the Ge concentration x in the alloy. In the limit of $x = 0$, we are regressing to the homoepitaxial case. Similar trends have been observed, for example, by RHEED in MBE growth of $In_xGa_{1-x}As$ on GaAs (Berger *et al.*, 1988).

The effect of deposition rate on surface morphology has not been studied systematically to our knowledge and is not well understood. Presumably, the deposited species will generally diffuse most easily as single surface adatoms; as the deposition rate increases, the probability that further deposited atoms

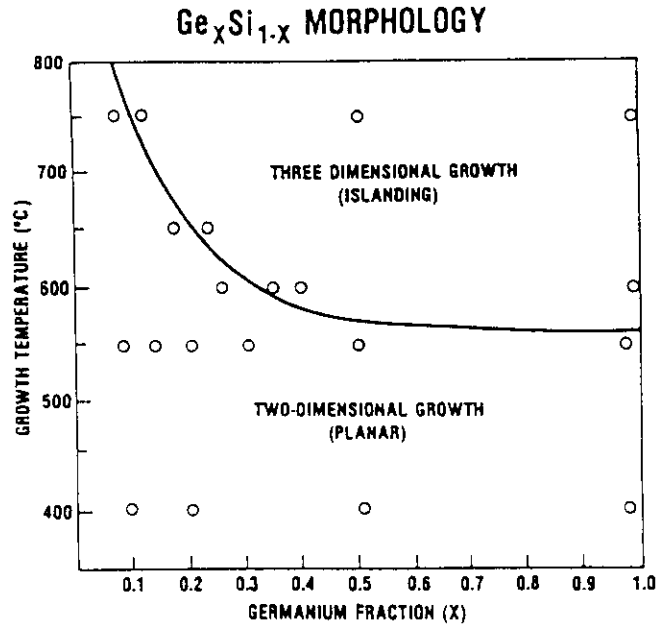

FIG. 10. Clustered versus layer-by-layer growth for MBE growth of Ge_xSi_{1-x} Si(100) (from Bean *et al.*, 1984).

will impinge upon and bond with the diffusing adatom before it reaches a stable cluster will increase. It might therefore be expected that higher deposition rates would effectively inhibit surface diffusion and reduce epilayer surface roughness. Evidence contrary to this hypothesis, however, comes from analysis of low-temperature photoluminescence (PL) studies in AlGaAs/GaAs/AlGAs quantum well structures (e.g., Bimberg *et al.*, 1986; Hayakawa *et al.*, 1985). In these structures, it is commonly found that interrupting growth for a time of the order of seconds to minutes at the heteroepitaxial interfaces (this might be regarded as the limit of a vanishingly small growth rate) significantly reduces the photoluminescence line width, as illustrated in Fig. 11 (Note that in the 100 sec spectrum in this figure, the peak has split into a fine doublet structure, attributed to two discrete well widths differing by one monolayer). It is generally believed that this corresponds to a planarization of the growth surfaces during interruption, a significant factor in the PL peak broadening being well-width variation, and hence variations in exciton energy, arising from interface roughness. It would thus appear that in this system, reducing the growth rate allows surface diffusion to reduce surface roughness. This apparent dichotomy might be resolved by considering the specifics of the AlGaAs/GaAs system, where the constituents are

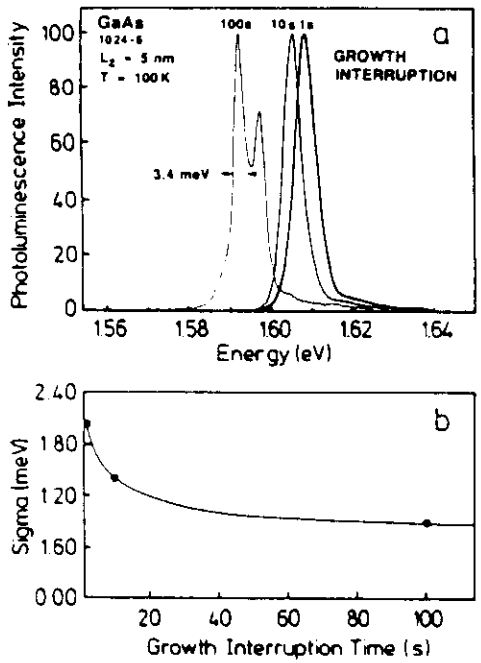

FIG. 11. (a) Comparison of $T = 100$ K photoluminescence spectra of 5 nm GaAs quantum wells grown between $Al_xGa_{1-x}As$ barriers, for growth interruptions at both sets of interfaces of 1, 10, and 100 seconds. Also shown (b) is the magnitude of line broadening as a function of growth interruption time (from Bimberg *et al.*, 1986).

closely lattice-matched, isostructural, and chemically similar. Thus, the thermodynamic driving forces for cluster deposition are relatively small or non-existent. In these growth-interruption experiments, a continuous film of, say, AlGaAs is likely to have formed over the preceding GaAs layer before the interruption. At this stage, energy is lowered in the only possible way, i.e., by minimization, in this case by planarization, of the free growth surface. The liquid-drop model discussed earlier and defined in Eq. (1) might thus be expected to apply only when a significant fraction of free substrate surface remains.

Surface morphology may thus also be regarded as a function of the deposited epilayer thickness, in that depending on the nucleation density, at some mean deposit thickness h_m, the substrate will attain complete substrate surface coverage. Further deposition will thus approximate the homoepitaxial case, where the epitaxial material is growing onto itself. At this stage, surface diffusion would be expected to act such as to *planarize* the surface, because the sole free surface is now the growth surface, whose energy

will be minimized for a minimum area, i.e., a single plane. Details of nucleation kinetics with temperature have been studied in many systems (e.g., Biegelsen *et al.*, 1987; Zinke-Almang *et al.*, 1987; Venables *et al.*, 1987); it is generally found that the nucleation density increases as substrate temperature and surface diffusion decrease, as illustrated in Fig. 12. Thus, at lower temperatures, the thickness h_m will be less than for higher temperatures, since individual nuclei require less lateral growth before coalescing with their neighbors. This is used to advantage in the growth of GaAs on Si, where the initial growth stages are highly three-dimensional (Biegelsen *et al.*, 1987; Hull and Fischer-Colbrie, 1987). In this system (e.g., Fischer *et al.*, 1985; Nishi *et al.*, 1985; Harris *et al.*, 1987), growth of GaAs normally proceeds with a low-temperature (~ 400°C) "buffer" layer of thickness of ~ 500–1000 Å, prior to

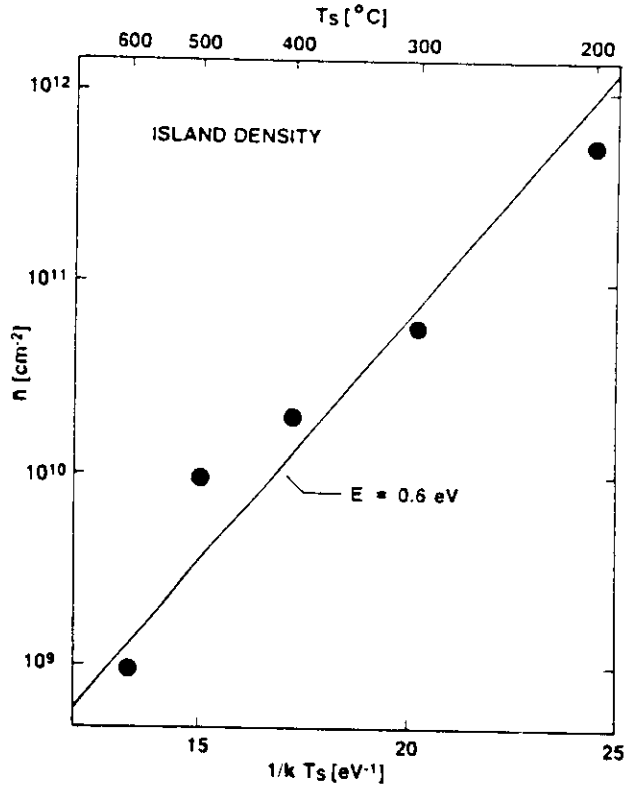

FIG. 12. Nucleation density for GaAs/vicinal Si(100) (2.5 degrees toward ⟨011⟩) as a function of substrate inverse temperature (Reprinted with permission from the Materials Research Society, from Biegelsen *et al.*, 1988.)

higher-temperature (~ 600 C) growth under conditions more appropriate to homoepitaxial GaAs. This buffer layer produces better surface morphology than uniform growth at the higher temperature, because the higher nucleation density produces more rapid substrate coverage and an earlier simulation of homoepitaxial conditions. In summary, it is indeed fortunate that the very conditions that produce clustered growth (significant surface diffusion) can act so as to repair the surface morphology if the deposited epilayer is significantly thick. Note, however, that in the example of GaAs/Si, individual nuclei are typically relaxed before they coalesce (e.g., Hull and Fischer-Colbrie, 1987) and thus strain is not playing a significant role in the coalescence process. It has been suggested (e.g., Grabow and Gillmer (1987) and Bruinsma and Zargwill (1987)) that island formation on a previously planar-strained epilayer can be coincident with the strain relaxation process, as in the Stranski–Krastanow transition. It appears that kinetics may defeat this process, however, under typical growth conditions of semiconductors.

The above "liquid-drop" model should, in general, be modified to include the effect of variation of surface energy over different surfaces in the epitaxial cluster. As the contact angle θ increases, so will the range of surface normal directions over the cluster. If the cluster contains only a very small number of atoms, it is unlikely that surface atoms will experience an environment that closely approximates to uniform surfaces of atoms in low index planes, because the orientations of tangential planes to the cluster surface will vary so rapidly over the cluster. As the clusters grow, however, larger and larger numbers of surface atoms will approximate low-index planes. At some critical size, the cluster might thus be expected to facet into low-index planes so as to minimize its surface energy; this process will be encouraged for high substrate temperatures and for systems, such as III-V compounds, where different low-index planes may have very different energies.

The above arguments are illustrated with reference to the $InAs_{0.2}Sb_{0.8}$/GaAs system in Figs 13–15. Figures 13 and 14 are respectively cross-sectional and plan-view TEM images of different stages of the $InAs_{0.2}Sb_{0.8}$/GaAs deposition process (Yen *et al.*, 1987; Hull *et al.*, 1988a). It can be seen from Fig. 13 that in the earliest stages of growth (average nominal epilayer thickness of ~ 50 Å), approximately hemispherical $InAs_{0.2}Sb_{0.8}$ clusters nucleate on the GaAs surface. As deposition continues, individual nuclei grow, and at a critical dimension, corresponding to a nucleus radius of ~ 200 Å, starts to exhibit strong surface facetting behavior. As can be seen from Fig. 13, the facetted nuclei correspond to trapezoids, with large surface areas exposed on the top (100) surfaces, and with the trapezoid edges corresponding to {111} faces. For compound semiconductors such as GaAs, two types of (111) surface exist: the column-III (or 111A) face and the column-V (or 111B) face. The (111)A and B faces are generally of different energies,

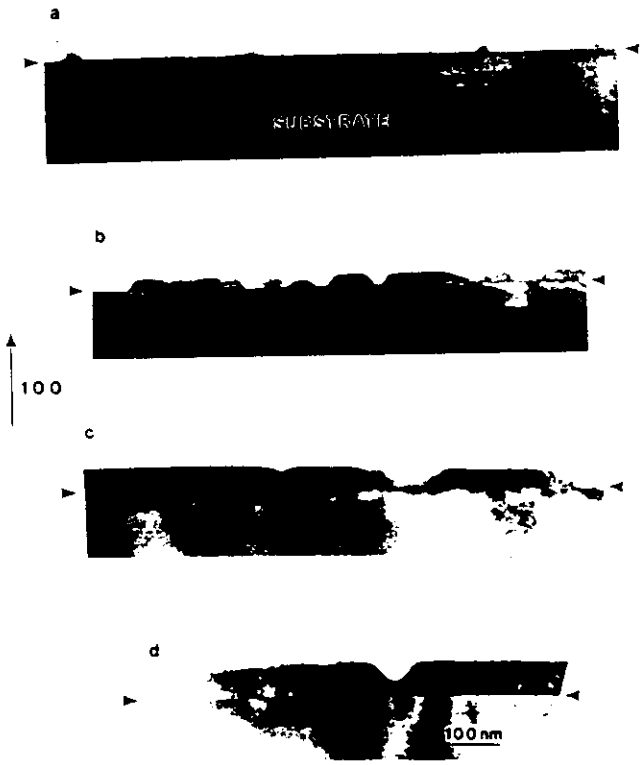

FIG. 13. Cross-sectional ⟨011⟩ TEM images of InAsSb alloys deposited on GaAs substrates. Nominal mean alloy thicknesses are: (a) 50 Å; (b) 100 Å; (c) 300 Å; (d) 600 Å. The substrate surface in each image is arrowed.

which often leads to anisotropically dimensioned facetted nuclei in epitaxial growth of III-V compound semiconductors (see, e.g., Pirouz *et al.*, 1988).

The extreme sensitivity of the nuclei dimensions to surface facetting is illustrated in Fig. 15, which plots the height, h, and the width, w, of individual nuclei versus their cross-sectional area, A. It can be seen that in the earliest stages of growth, the nuclei are approximately hemispherical, i.e., $w \sim 2h$. As the nuclei pass through a critical value of $A \sim 100{,}000$ Å^2, growth along the substrate normal almost arrests, and further growth is almost entirely lateral. In this regime, $dw/dA \sim 10(dh/dA)$. The enhanced lateral growth corresponds to the extension of the (100) trapezoid top and the long trapezoid edges of lower energy {111} with respect to the higher energy {111} short trapezoid edges. When lateral growth has been sufficient so that neighboring nuclei

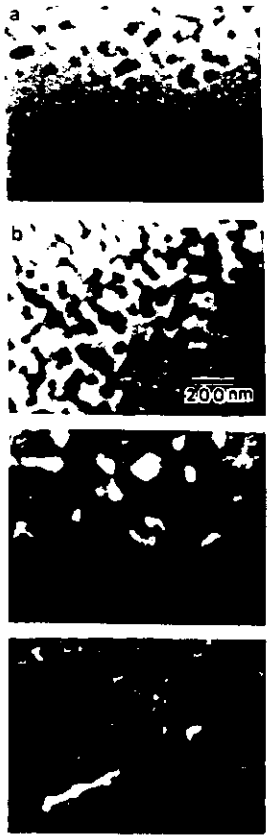

FIG. 14. Plan-view TEM images of InAsSb alloys deposited on GaAs substrates. Nominal mean alloy thicknesses are: (a) 50 Å; (b) 100 Å; (c) 300 Å; (d) 600 Å. The lighter areas in each image correspont to uncovered substrate.

have coalesced and the substrate surface has been approximately entirely covered, further lateral growth of the deposit is not possible, and further growth has to be along the surface normal. This happens at a mean substrate deposit thickness of ~ 300 Å.

The above experiments were carried out for substrate temperatures of 500°C, which are very near the InSb melting point of 550°C. Thus, we would expect very high surface diffusivities and almost equilibrium surface cluster conditions to apply. It is interesting, and conceivably of practical importance, that the very conditions that promote surface clustering in this system also generate a self-planarizing mechanism. The very different surface energies of a compound semiconductor such as InAsSb, in this case, have produced dramatic surface facetting and enhanced lateral growth. Thus, by a mean deposit thickness of only 300 Å, a system that was initially highly three-dimensional has converted to a relatively planar surface morphology. These

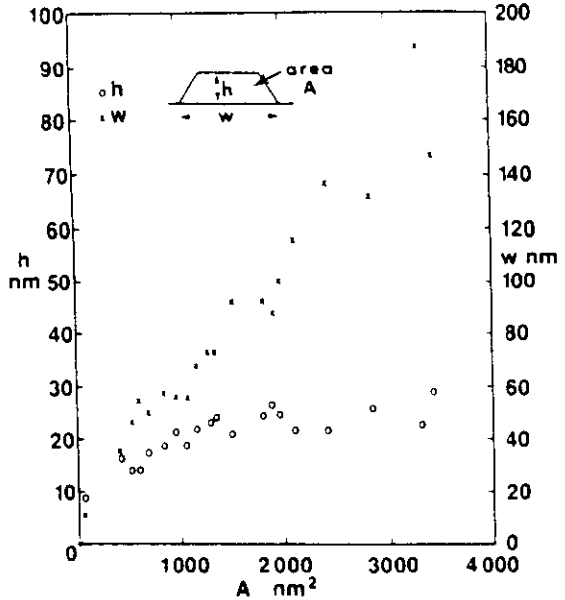

FIG. 15. Graphs of measured island height, h, and island width, w, versus island cross-sectional area, A. All measurements are from cross-sectional TEM images of nominal 100 Å and 300 Å InAsSb thickness samples. Error bars are not shown in the figure for clarity; the estimated errors on h and l are $\sim \pm 20$ Å. Experimental points for island height are denoted by dots, and for island width by crosses.

trends are in qualitative agreement with RHEED patterns in this thickness regime, which show the corresponding transition from sharp to streaked diffraction peaks (Yen *et al.*, 1987).

V. Strain Relief in Lattice-Mismatched Epitaxy

A. Introduction

It has long been recognized that, in principle, it is possible to grow coherent lattice-mismatched epitaxial structures, where the lattice parameter of the deposit is different from that of the substrate (Nabarro, 1940; Mott and Nabarro, 1940; Frank and Van der Merwe, 1949a,b,c). This concept is illustrated in Fig. 16. In lattice-matched heteroepitaxy (Fig. 16a), the deposit and the substrate have the same lattice parameter, and deposition of the epilayer atoms onto the substrate surface allows them to easily locate the potential minima corresponding to the substrate lattice sites, assuming they have sufficient thermal energy (i.e., if the growth temperature is high enough)

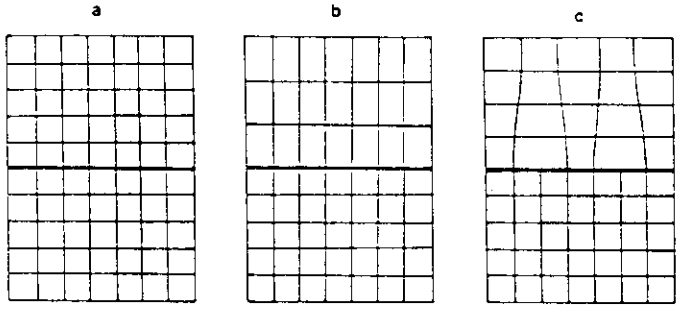

FIG. 16. Schematic illustration of (a) lattice-matched heteroepitaxy; (b) coherently strained lattice-mismatched heteroepitaxy; (c) relaxed lattice-mismatched heteroepitaxy. (Reprinted with permission from Plenum Pub. Corp., from Hull *et al.*, 1989d.)

to move to the nearest minimum. In strained-layer epitaxy (Fig. 16b), despite the difference in substrate and deposit lattice parameters, deposit atoms are constrained to the substrate interatomic spacings in the plane of the interface. We designate such structures commensurate or coherent. Significant elastic strain energy is stored in the structure (accommodation of a lattice mismatch of just 1% in this fashion produces a stress field equivalent of 2 GPa, assuming a shear modulus of 5×10^{10} Pa and a Poisson's ratio of 0.33). A tetragonal distortion of the unit cell of the deposit is also produced, since elasticity theory shows that the planar stress parallel to the interface, σ_i, will produce a normal strain ε_n given by:

$$\varepsilon_n = \frac{1+\nu}{1-\nu}\varepsilon_i. \tag{2}$$

Here ν is Poisson's ratio, and ε_i is the interfacial strain produced by accommodation of the lattice mismatch, equal to $\sim(a_e - a_s)/a_s$, where a_s and a_e are the substrate and epilayer bulk (relaxed) lattice parameters, respectively. These relationships assume effectively that the substrate is of infinite thickness, such that all the elastic strain energy is stored in the deposit. In practice, the thickness of the substrate (typically $\sim 5 \times 10^{-4}$ m) is very much greater than the epilayer thickness (Å to microns), so this approximation is reasonably valid. In deposition onto thin film substrates, corrections have to be made for the finite substrate thickness.

For a given lattice mismatch, the elastic strain energy in the coherent deposit will increase approximately linearly with the substrate thickness. When the strain energy is sufficiently large, it will start to be relieved by deformation of the hitherto coherent structure. This process occurs via the introduction of slipped regions into the crystal, bounded by line defects

known as "misfit" dislocations. As shown in Fig. 16c, these act so as to effectively remove planes of atoms from the deposit if the epilayer is of larger lattice parameter than the substrate (if the epilayer has the smaller lattice parameter, then extra planes will be effectively introduced into the deposit). The removal of these atomic planes increases the average spacings between deposit atoms, allowing the epilayer to relax toward its bulk structure. We designate such structures semicoherent or discommensurate.

B. Review of General Dislocation Properties

Before giving a more detailed description of present understanding of the strain relaxation process via the introduction of misfit dislocations, we will now briefly review the known salient properties of dislocations. Much classic work in this field has been done (see, e.g., Hirth and Lothe, 1968, and Nabarro, 1967), particularly in metals. The primary technique for experimental study of dislocation microstructure is TEM, as pioneered by Hirsch and co-workers (Hirsch *et al.*, 1977).

A perfect or total dislocation may be viewed as the boundary surrounding a slipped region of a crystal. As such, it is a line defect. It is a geometrical property of a perfect dislocation that it cannot simply terminate in the bulk of a crystal, but must rather terminate at a free surface, or upon itself by forming a continuous loop, or at a node with other defects. The structure of a dislocation is determined by its line direction, **L**, and by its Burgers vector **b**. The Burgers vector is defined by the direction and magnitude of the closure failure of a rectilinear loop drawn around the dislocation line. For a total or perfect dislocation, the Burgers vector links two atomic sites in the unit cell. The Burgers vectors of total dislocations in the cubic semiconductors discussed in this chapter are almost always $\frac{1}{2}\langle 011\rangle$. The Burgers vector of a given dislocation is constant anywhere along that dislocation apart from a possible change in sign, according to convention. If **b** is parallel to **L**, then the dislocation is said to be of the screw type, whereas if **b** and **L** are orthogonal, the dislocation is of the edge type. Any intermediate configuration is said to be mixed screw and edge. Since a dislocation is not constrained to be straight, its screw/edge character (but not its Burgers vector) can change along its length.

Dislocations move on a given set of planes known as slip planes; in the cubic semiconductors considered here, these are $\{111\}$ planes. For a (100) interface, these planes make $[011]$ or $[01\bar{1}]$ intersections with the interface; thus, misfit dislocations typically lie in a square mesh along these directions. If the dislocation Burgers vector lies within its slip plane, it may move by a low-energy cooperative process known as glide. This process involves no mass transport of atoms and is thus relatively rapid. If a dislocation has its Burgers vector out of the slip plane, then it must move by a process known

as climb, which involves mass transport of either vacancies or interstitials. Thus, this is generally a much slower process than glide.

The specific configurations of misfit dislocations to be considered here are shown in Fig. 17. For a (100) interface, consider for example the $(\bar{1}11)$ slip plane. This will intersect the interface along the $[01\bar{1}]$ direction. Total dislocations of $\mathbf{b} = \frac{1}{2}[101]$ or $\frac{1}{2}[110]$ will lie in this slip plane and thus be able to move by glide. Since **b** is neither parallel nor perpendicular to **L**, these are mixed dislocations. Their Burgers vectors lie at an angle of 60 degrees to the interface and to their line directions (they are often referred to as 60-degree dislocations); thus, their component in the interfacial plane is only $\frac{1}{2}$. For this reason, these dislocations are only 50% effective (as a fraction of their total Burgers vector magnitude) in relieving lattice mismatch. Dislocations of the type $\frac{1}{2}[01\bar{1}]$, however, will have **b** perpendicular to **L** (edge or 90-degree dislocations), and their Burgers vectors will be 100% effective at relieving lattice mismatch. Since their Burgers vectors lie outside the slip plane, they must move by climb. Thus, although they may be regarded as more efficient than 60-degree dislocations, they will grow more slowly. The final possibility of screw-type $\frac{1}{2}[01\bar{1}]$ dislocations may be discounted, because they do not relieve any lattice mismatch in this configuration.

The deformation around the dislocation line is very well described by classic elastic theory, apart from the region very close to the dislocation center, known as its core. In this region, atomic displacements are sufficiently high so that Hooke's law is invalidated, and the total dislocation energy is given by the elastic energy outside of the core (which may be accurately

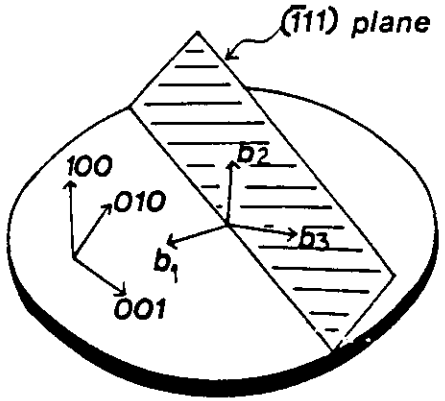

$\underline{b_1} = \frac{1}{2}[0\bar{1}1]$

$\underline{b_2} = \frac{1}{2}[110]$

$\underline{b_3} = \frac{1}{2}[101]$

FIG. 17. Schematic illustration of the misfit-dislocation configurations encountered in cubic semiconductors at (100) interfaces.

calculated and is proportional to b^2), plus the energy within the core, which is not well known. The size of the core region is very small, being confined in semiconductors to a radial coordinate $< b$ from the deformation center.

The strain field around a dislocation produces a stress field. This field may act either upon the dislocation itself if it is curved (this gives rise to the concept of dislocation line tension), upon point defects, upon a free surface (giving rise to the concept of an image force), or upon other dislocations, causing interdislocation interactions. The force that two dislocations A and B exert on each other is proportional to the dot product of their Burgers vectors, $\mathbf{b}_A \cdot \mathbf{b}_B$, and is inversely proportional to the distance between them.

Finally, a total dislocation may dissociate into partial dislocations of lower magnitude Burgers vector. In the absence of external stress fields, this will be energetically favorable if the sum of the squares of the partial Burgers vectors is less than the square of the original total Burgers vector. The Burgers vectors of partial dislocations do not link lattice sites and thus produce stacking faults. For cubic semiconductors, $\frac{1}{6}\langle 112\rangle$ and $\frac{1}{3}\langle 111\rangle$ are the partial Burgers vectors most commonly observed. In a dissociation reaction, the partial dislocations will move apart producing a stacking fault between them. Their equilibrium separation will then be determined by the stacking fault energy. The total Burgers vector is always conserved in any such dissociation reaction. Note that other dislocation reactions are also possible involving total and/or partial dislocations, the criteria being that the total energy of the system is reduced and that the total Burgers vector is conserved.

C. Critical Thickness

It might be expected that there will be a characteristic epilayer thickness (for a given lattice mismatch) at which the commensurate–discommensurate transition occurs, or at least dramatically accelerates. The magnitude of this "critical thickness," h_c, will be related to the balance between the relief of strain energy and the extra energy associated with the lattice distortions produced by the misfit dislocations. A number of equilibrium theories have been developed to attempt to describe h_c as functions of the elastic mismatch and the elastic constants of an epitaxial system. Early models by Frank and Van der Merwe and co-workers (Frank and Van der Merwe 1949a,b,c; Van der Merwe and Ball, 1975) attempted to model the commensurate–discommensurate transition by minimizing the energy of a misfit dislocation array at the interface. These formulations were originally developed for consideration of body-centered cubic metal systems. They are mathematically rigorous and have no analytical solutions. Different approximations are required for solution in the thin and thick epitaxial film limits (dimensions are defined here relative to the spacings of the misfit-dislocation

arrays). Matthews and Blakeslee (Matthews and Blakeslee 1974a,b; Matthews, 1975) developed models for strain relaxation in epitaxial III-V compound semiconductor systems. In the most commonly quoted formulation of this model, they assumed that the source of misfit dislocations was the density of pre-existing "threading dislocations" in the compound semiconductor substrate. At the time of the original formulation of the Matthews and Blakeslee models, the threading-dislocation density in commercially available III-V substrates was of the order of $10^6\,\mathrm{cm}^{-2}$, producing a sufficiently high-density source for the misfit-dislocation process. Relaxation of the epilayer was predicted to occur via glide of the original threading dislocations akong the strained interface, as illustrated schematically in Fig. 18. To analyze the conditions required for this process to occur, Matthews and Blakeslee considered the forces acting on the laterally propagating threading arm. The force that drives extension of the misfit dislocation along the interfacial plane is the force due to the misfit stress in the structure, F_σ. Competing with this is the force due to the misfit-dislocation line tension, F_T. This force essentially represents the fact that as different segments of a curved dislocation exert a force on each other, extending the length of the dislocation requires work to be done against the stress field exerted by other dislocation segments (see Hirth and Lothe, 1968, for a complete discussion). The condition for misfit-dislocation propagation is then simply that $F_\sigma > F_T$; the epilayer thickness where $F_\sigma = F_T$ may be regarded as the critical thickness where misfit dislocation propagation begins to occur.

Simple elasticity theory yields

$$F_\sigma = \mathrm{S2Gbh}\frac{(1+\nu)}{(1+\nu)}\varepsilon, \tag{3}$$

where G, h, and ν are the shear modulus, thickness, and Poisson ratio, respectively, of the epitaxial deposit, $\mathbf{b}$ is the dislocation Burgers vector, S is an angular factor resolving the misfit stress on the glide direction, and ε is the strain due to the mismatch between the lattice parameters of epilayer and substrate.

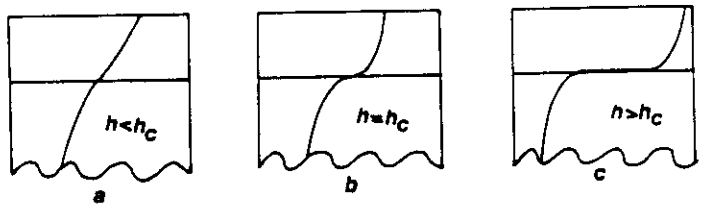

FIG. 18. Schematic illustration for the Matthews and Blakeslee model of misfit-dislocation propagation.

The line-tension force, F_T, is configuration dependent. An appropriate expression for the magnitude of this force for the threading-dislocation configuration is

$$F_T = \frac{Gb^2(1-\nu\cos\theta^2)}{4\pi(1-\nu)}\ln\left(\frac{\alpha h}{b}\right). \tag{4}$$

where θ is the angle between the threading-dislocation line and its Burgers vector, and α is a constant representing the dislocation-core energy (α is generally taken to be 4 for covalent semiconductors; see Hirth and Lothe, 1968).

Equating (3) and (4) enables a solution for the critical thickness $h = h_c$. This original Matthews and Blakeslee formulation appears appropriate for the substrate threading-dislocation mechanism they propose, and has been experimentally verified for III-V compound semiconductor strained-layer epitaxy (see, e.g., Fritz *et al.*, 1985), as illustrated in Fig. 19. Extension of this

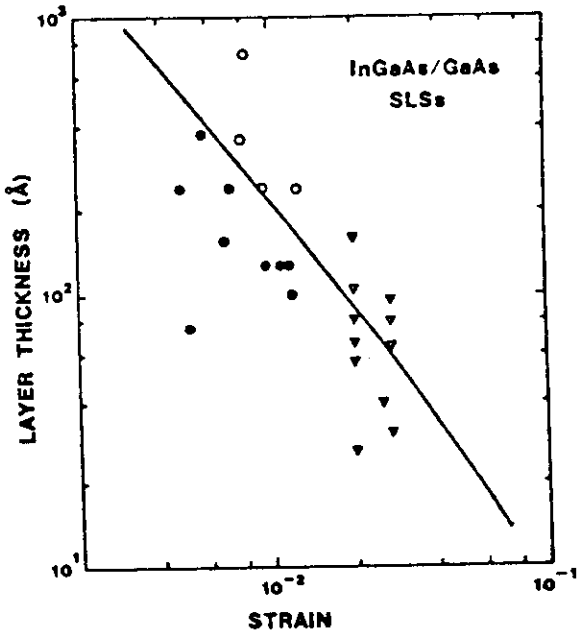

FIG. 19. Critical-thickness measurements as a function of composition in the $In_xGa_{1-x}As/GaAs(100)$ system (from Fritz *et al.*, 1985). Solid points correspond to misfit-dislocation-free structures and open points to dislocated structures. Solid line is from theory of Matthews (1975).

model to systems such as those grown on Si substrates where there is not a high threading-dislocation density in the substrate, however, may not be appropriate as the activation barriers for dislocation nucleation and motion may prevent the essentially equilibrium configuration predicted by the Matthews–Blakeslee formulation from being attained (the nucleation barrier for the substrate threading-dislocation configuration will be zero). Such a discrepancy is illustrated in Fig. 20, where experimental data for strained-layer Ge_xSi_{1-x}/Si(100) critical-thickness transitions are shown. Two different curves are shown for substrate temperatures of 550°C (Bean *et al.*, 1984) and 750°C (Kasper *et al.*, 1975), respectively. It can be seen that critical thicknesses are dramatically reduced at the higher substrate temperature. As discussed later in this section, we interpret this temperature dependence as being due to the activation barriers that have to be overcome for dislocation nucleation and motion. Also shown in Fig. 20 are the predictions of the Matthews and Blackeslee model for the "equilibrium" critical thickness. It should be noted that the exact form of this curve depends upon both the dislocation configuration and its structure (Burgers vector). Here we draw the curve appropriate to a $\frac{1}{2}\langle 011\rangle$ dislocation of 60 degree character (i.e., with its Burgers vector lying within its glide plane) and in a hexagonal half-loop configuration, with one side of the semihexagon lying in the interfacial plane, and the other sides threading to the growth surface.

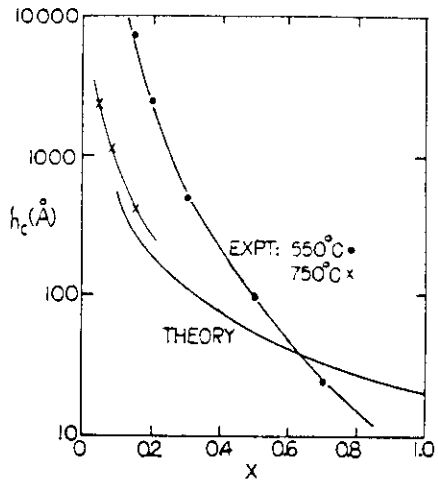

FIG. 20. Critical-thickness measurements in the GeSi/Si system (from Bean *et al.*, 1984; 550°C; Kasper *et al.*, 1975, 750°C), with equilibrium predictions of Matthews–Blakeslee theory. (Reprinted with permission from Elsevier Sequoia S. A., Hull, R., Bean, J. C., Eaglesham, D. J., Bonar, J. M., and Buescher, C. (1989), *Thin Solid Films* **183**, 117.)

The discrepancy between experiment and equilibrium theory is apparent. It should also be noted that, as has been pointed out by Fritz (1987), the exact positions of the experimental curves will depend on the sensitivity of the technique used to detect strain relaxation. The curves of Fig. 20 were determined using Rutherford backscattering (RBS) X-ray diffraction, and plan-view TEM, which are probably sensitive to strain relaxation of the order of one part in 10^3. More sensitive techniques would probably cause both experimental curves to fall at lower critical thicknesses. This effect has been experimentally verified in the InGaAs/GaAs system (Gourley *et al.*, 1988), where it has been shown that application of a technique (in this case PL imaging) that is able to detect very low dislocation densities may reveal the onset of misfit-dislocation formation at epilayer thicknesses significantly less than those inferred by lower sensitivity techniques (e.g., RBS or TEM). Similar results have been demonstrated via X-ray topography in the GeSi/Si system (Eaglesham *et al.*, 1988).

An elegant model that accounts for the temperature dependence of strain relaxation has recently been developed by Dodson and Tsao (Dodson and Tsao, 1987; Tsao *et al.*, 1987). The model assumes the velocity of misfit dislocations, once nucleated, to be proportional to the excess stress in the strained epilayer. This excess stress is defined as the actual stress within the epilayer minus the residual stress that would be expected in the equilibrium state of the system. This excess stress may be derived straightforwardly in the framework of the Matthews and Blakeslee model as the stress due to the lattice mismatch, as obtained from Eq. (3), minus the self stress produced by the line tension in Eq. (4). If a dislocation source term (not explicitly identified in this model) is assumed, the solution of the relevant dynamic equations allows the strain state of the system to be predicted as functions of layer dimensions and compositions, and the growth temperature and time. Using bulk activation energies for dislocation glide in Si and Ge (Alexander and Haasen, 1968; Patel and Chaudhuri, 1966), this model has successfully predicted a wide range of experimental data in the Ge_xSi_{1-x}/Si(100) system (Dodson and Tsao, 1987), where equilibrium theories have not described experimental results well. If the relevant experimental data for dislocation glide energies and elastic constants exist, then this model should be equally applicable to any other strained-layer system.

D. Details of the Strain Relaxation Process

1. Introductory Remarks

Precise application of a kinetic theory such as the Dodson–Tsao model, however, requires detailed knowledge of dislocation nucleation mechanisms, activation energies for nucleation and propagation, knowledge of the precise

dislocation configuration (Burgers vector, line direction, and dissociation state), and the details of defect interactions. Experimental and theoretical understanding of these various processes is still incomplete.

The main stages in relaxation of elastic strain via introduction of misfit dislocations are shown in Fig. 21. In Fig. 21a, dislocations are nucleating. In the absence of significant dislocations pre-existing in the substrate, this nucleation stage is perhaps the least understood event in the relaxation process. Given the requirement that a dislocation terminate upon itself at a node with another dislocation or at a free surface, the three generic possibilities for nucleation within the epitaxial layer of the first dislocations are shown: nucleation of a complete loop at a point within the epitaxial layer or at the substrate–epilayer interface, or nucleation of a half-loop at the free growth surface. In Fig. 21b, these initial loops are shown expanding such that the length of misfit dislocation in the substrate–epilayer interfacial plane is growing. Finally, the dislocation population will become high enough so that adjacent defects will interact, modifying their energy balance (Fig. 21c).

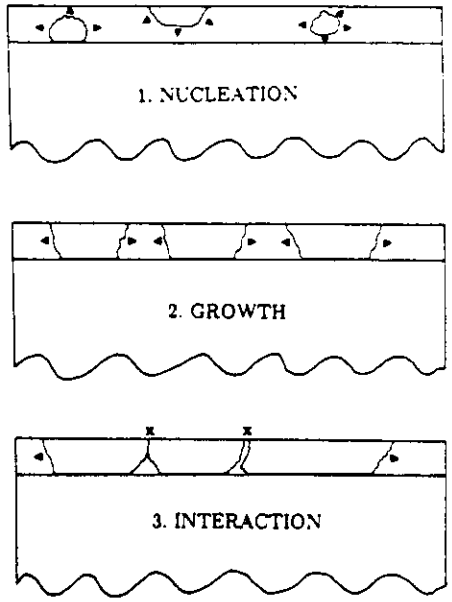

FIG. 21. Schematic illustration of (1) nucleation, (2) growth, and (3) interaction of misfit dislocations. (Reprinted with permission from Plenum Pub. Corp., from Hull *et al.*, 1989d.)

2. Nucleation of Misfit Dislocations

To illustrate the difficulties associated with the nucleation of misfit dislocations, consider the activation energy required to nucleate a half-loop at the growth surface. As a function of the loop radius, the total loop energy, $E_{tot}(r)$, will be given generically by the relationship

$$E_{tot}(r) = E_{self}(r) - E_{\sigma}(r) \pm E_{step}(r) - E_{dis}(r). \quad (5)$$

Here $E_{self}(r)$ is the self energy of the dislocation loop, $E_{\sigma}(r)$ is the strain energy relaxed by the dislocation loop, $E_{step}(r)$ is the energy associated with possible creation or removal of a surface step, and $E_{dis}(r)$ is the energy associated with possible dissociation of the total dislocation into partials. The exact forms of these individual components depend on the specific dislocation microstructure but have been evaluated for different systems and configurations by several authors (e.g., Matthews *et al.*, 1976; Fitzgerald *et al.*, 1989; Eaglesham *et al.*, 1989; Hull and Bean, 1989a). The calculated loop energy generally passes through a maximum or activation barrier, δE, at a critical loop radius, R_c. The magnitude of R_c is typically of the order of 10–100 Å for common lattice mismatches of, say, 0.3–3%. The activation barriers generally become of the order of a few eV or less at strains $> \sim 4$–5%, making this nucleation process energetically feasible, but are extremely high (tens or even

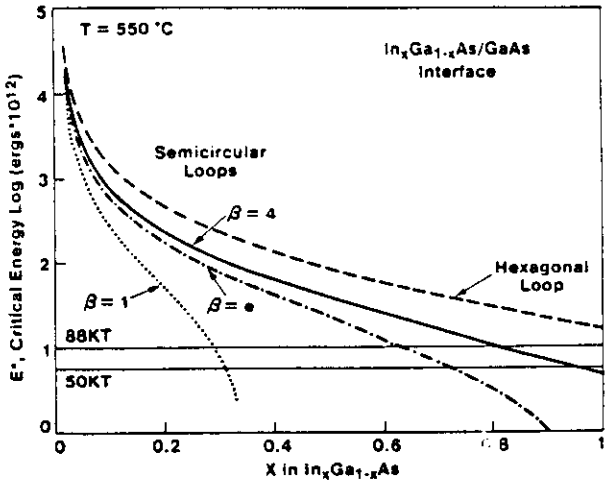

FIG. 22. Activation barriers for the nucleation of a surface half-loop in the $In_xGa_{1-x}As/GaAs$ system (from Fitzgerald *et al.*, 1989). Different values of β correspond to different estimates of the dislocation core energy (see Hirth and Lothe, 1968; Eaglesham *et al.*, 1989).

hundreds of eV) for more moderate stresses of $< \sim 1\%$, as illustrated for $In_xGa_{1-x}As/GaAs$ in Fig. 22. Similar numbers are obtained for the GeSi/Si system (Eaglesham *et al.*, 1989; Hull and Bean, 1989a). It thus appears that in the relatively low mismatch regime, alternative nucleation sources have to be sought. Note that nucleation of full loops within the epilayer or at the epilayer–substrate interface would be expected to produce higher activation barriers, due to the necessity to nucleate a complete loop, as opposed to a half-loop at the surface.

Little work exists to date in establishing alternative nucleation paths. In a detailed analysis of dislocation densities in finite InGaAs pads grown on GaAs substrates, Fitzgerald *et al.* (1989) deduced that dislocation nucleation is due to "fixed" sources, i.e., sources inherent to the substrate or growth-chamber geometry such as substrate threading dislocations, oval defects, or particulates. Hagen and Strunk (1978) have proposed that intersection of orthogonal dislocations with equal Burgers vectors can produce a regenerative multiplication mechanism, a process that has been identified in several systems (Hagen and Strunk, 1978; Chang *et al.*, 1988; Rajan and Denhoff, 1987; Kvam *et al.*, 1988). This process, however, still cannot explain the generation of the initial defect density necessary to produce the observed intersection events. Eaglesham *et al.* (1989) have detected a novel generation mechanism in low-mismatch ($< 1\%$) GeSi/Si systems, consisting of the dissociation of $\frac{1}{6}\langle 114\rangle$ diamond-shaped loops. In the same system, Hull *et al.* (1989a) have measured a relatively low activation energy of 0.3 ± 0.2 eV for $Ge_{0.25}Si_{0.75}/Si(100)$ and have suggested that this may be associated with clustering of atoms in the alloy epilayer (Hull and Bean, 1989a). A widespread and detailed understanding of this nucleation process, however, is still clearly lacking and may be unique to particular systems and growth conditions, and even to specific growth chambers.

3. *Direct Observations of Dynamic Misfit-Dislocation Events*

Detailed understanding of the strain relaxation process has been hampered by the absence of direct techniques for observing dynamic misfit-dislocation phenomena. We have recently developed techniques for in situ relaxation experiments in a TEM that allow real-time observation of misfit-dislocation nucleation, propagation, and interaction phenomena.

The experimental configuration for these experiments is shown in Fig. 23. A suitable strained $Ge_xSi_{1-x}/Si(100)$ structure is grown in the MBE chamber at a substrate temperature of 550°C. The epilayer thickness is designed to lie between the equilibrium value of h_c (Matthews, 1975) and the experimentally measured value (Bean *et al.*, 1984) for this substrate temperature. Thin plan-view TEM samples are then fabricated, and the thinned structure is subsequently annealed inside the electron microscope. While the annealing temperature is raised to the growth temperature and above, the essentially

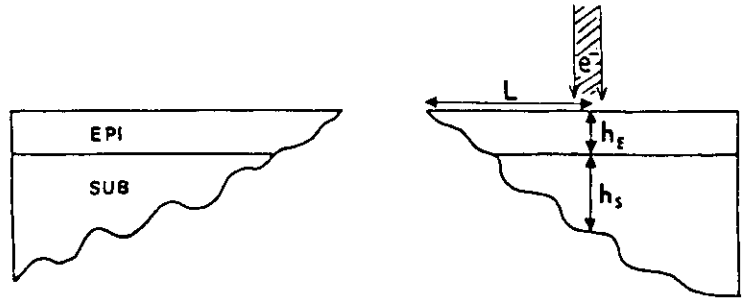

FIG. 23. Schematic illustration of the experimental geometry for TEM in situ strained-layer relaxation experiments. (Reprinted with permission from Plenum Pub. Corp., from Hull *et al.*, 1989d.)

metastable 550°C structure relaxes as dislocations nucleate and then grow. Both static (photographic negative) and dynamic (video) images of the relaxation process may be recorded. Thus, the various strain relaxation processes (dislocation nucleation, growth, and interaction) may be observed directly and in real-time. As described in detail in Hull *et al.* (1988b), the crucial experimental complication is careful consideration of thin-foil relaxation effects in the TEM sample. Consideration of such effects leads to the conclusion that films of Ge composition $x \sim 0.25$–0.30 a few hundred Å thick represented the optimum geometry because (i) layer thicknesses are much less than the maximum thinned substrate thickness penetrable by imaging electrons, and (ii) surface roughness is negligible. Samples are always prepared in the plan-view geometry for these experiments, because annealing in the cross-sectional geometry would leave open the question of surface diffusion across heteroepitaxial interfaces at the top and bottom thin-foil surfaces. In the plan-view geometry, the Ge_xSi_{1-x}–Si interface is buried away from any free surfaces.

Plan-view TEM images of a typical annealing sequence are shown in Fig. 24. The dislocation density is observed to increase with annealing temperature. In Fig. 25, we show the average measured spacing between dislocations as a function of annealing temperature for two different sample thicknesses. It is observed that for $x = 0.25$, relaxation of $Ge_xSi_{1-x}/Si(100)$ heterostructures is relatively slow and continuous over the temperature range 550–900°C. As expected, the thinner epilayer relaxes more slowly, because its effective stress is less.

4. *Misfit-Dislocation Propagation*

By direct observation of dislocation motion via a video camera, image intensifier, and video recorder, we are able to directly measure dislocation velocities as a function of temperature. The time resolution of these

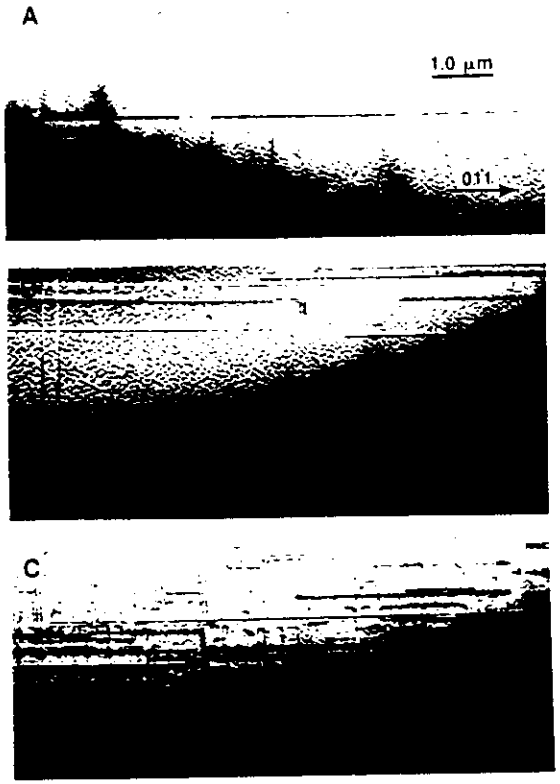

FIG. 24. Plan-view TEM images of a 350 Å $Ge_{0.25}Si_{0.75}$/Si(100) structure (a) as-grown at 550°C; (b) annealed to 700°C; and (c) annealed to 900°C (from Hull *et al.*, 1988b).

experiments is an individual TV frame, i.e., $\frac{1}{30}$sec. The minimum magnification we obtain on the viewing screen with the microscope objective lens excited is $\sim 45{,}000\times$ ($1500\times$ on microscope screen and $30\times$ on video viewing screen via camera). Thus, we may measure dislocation velocities from $\ll 1$ micron sec^{-1} to ~ 100 micron sec^{-1}. The dislocation velocities we observe are typically of the order 1000 Å – 1 micron sec^{-1} at the growth temperature of 550°C, rising dramatically with annealing temperature until they are > 100 micron sec^{-1} at 800°C. The measured dislocation velocity at the growth temperature immediately tells us something of great importance about metastability in this system: Even ignoring questions of misfit-dislocation nucleation and interactions, the low growth-temperature velocity severely limits strain relaxation. Thus, for the structures studied here, a

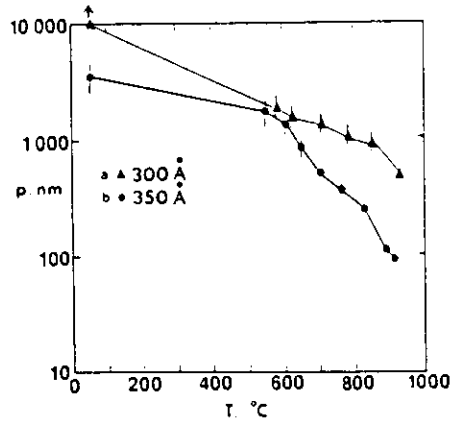

FIG. 25. Variation of average distance between misfit dislocations, p, versus annealing temperature, T, during relaxation of $Ge_{0.25}Si_{0.75}$/Si(100) structures (Hull *et al.*, 1988c. Reprinted with permission from "Dislocations and Interfaces in Semiconductors," eds. K. Rajan, J. Narayan, and D. Ast, 1988, Metallurgical Society, 420 Commonwealth Drive, Warrendale, PA 15086.)

sample thickness of 350 Å and a growth rate of ~ 3 Å sec^{-1} implies a maximum misfit dislocation length of ~ 0.1 mm. Since this is very much less than the wafer diameter, the ends of the misfit dislocation have to terminate at the nearest free surface, which in general is the growth surface. These dislocation ends thus constitute so-called threading dislocations, which are so deleterious to transport/optical properties and device performance in the epilayer. In the Ge_xSi_{1-x}/Si(100) system, they arise naturally as a result of the finite velocities of propagating dislocations.

Note that the above estimate of maximum dislocation length is very much an upper limit. In practice, measured dislocation lengths will be much lower, because (i) only for part of the growth time will the epitaxial film be obove the equilibrium critical thickness that will produce an excess stress to drive dislocation growth, (ii) misfit-dislocation kinetics are known to be partially nucleation limited in this system (Eaglesham *et al.*, 1989; Hull and Bean, 1989a), and (iii) as will be discussed later, dislocation interactions largely limit growth. These combined factors actually limit the average length of misfit dislocations in the $Ge_{0.25}Si_{0.75}$/Si(100) structures discussed above to ~ 10 microns (Hull *et al.*, 1989a).

Temperature-dependent in situ measurements of the glide velocities of non-interacting 60° dislocations suggest activation energies that are generally of the same order as those expected from interpolation of measurements in bulk Ge and Si (1.6 and 2.2 eV, respectively, e.g., Alexander and Haasen (1968) and Patel and Chaudhuri (1966)). However, we have measured

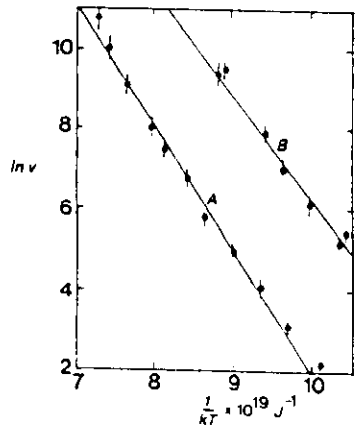

FIG. 26. Arrhenius plots of natural logarithm of dislocation glide velocity (velocities in Å sec^{-1}) vs. inverse energy for (A) 1200 Å $Ge_{0.15}Si_{0.85}$ buried beneath a 3000 Å Si(100) cap and (B) a surface layer of 600 Å $Ge_{0.28}Si_{0.72}$ on Si(100) (from Hull *et al.*, 1989a).

dislocation velocities in very thin and highly stressed Ge_xSi_{1-x}/Si(100) structures where activation energies are a few tenths of an eV less than expected from bulk measurements, as illustrated in the Arrhenius plots of Fig. 26. Possible models for this apparent activation energy lowering are: (i) a stress dependence of the "Peierls" (Peierls, 1940) or glide activation energy barrier (Dodson, 1988a) and (ii) propagation of the dislocation by nucleation of single "kinks" (see Hirth and Lothe, 1968) at the free epilayer surface as opposed to the classic bulk double kink nucleation mechanism. We also note that in more relaxed films where dislocation interactions become more significant, apparent glide activation energies may be further reduced (Hull *et al.*, 1989a). Also shown in Fig. 26 are in situ glide velocity measurements from a Ge_xSi_{1-x} layer buried beneath a Si cap. In these structures, we generally observe activation energies equivalent to the bulk values and velocities that appear to be substantially lower than in uncapped Ge_xSi_{1-x} layers, assuming a linear dependence of dislocation velocity on excess stress (Dodson and Tsao, 1987). Further work will be necessary to determine the precise defect propagation mechanisms.

We are not aware of any similar measurements of misfit-dislocation velocities in strained-layer compound semiconductor structures. In principle, the experiments we have described earlier could be applied to such materials in a relatively narrow temperature range between the original sample growth temperature and the temperature at which surface desorption (of, e.g., P or As) starts to significantly affect the surface stoichiometry.

5. *Dislocation Interactions*

It has been shown by Dodson (1988b) that interaction of high densities of misfit dislocations can significantly slow the rate at which a strained structure will relax. By experimentally measuring and theoretically modelling the rate at which a strained InAsSb/InSb with different types of compositional grading relaxed, it was shown that a simple "work-hardening" approach to misfit-dislocation interactions was reasonably successful at describing experimental data.

The importance of dislocation interactions has also been demonstrated by in situ GeSi/Si relaxation experiments (Hull *et al.*, 1989a; Hull and Bean, 1989b). Shown in Fig. 27 are the variation of average dislocation spacing, p, average density of misfit dislocations, N, and average misfit-dislocation length, L (calculated from a from a simple geometrical relationship linking p, N, and L as described in Hull *et al.*, 1989a), versus temperature during thermal relaxation of a $Ge_{0.25}Si_{0.75}$/Si(100) film. It can be seen that although N increases and p decreases with temperature as expected, L does not increase

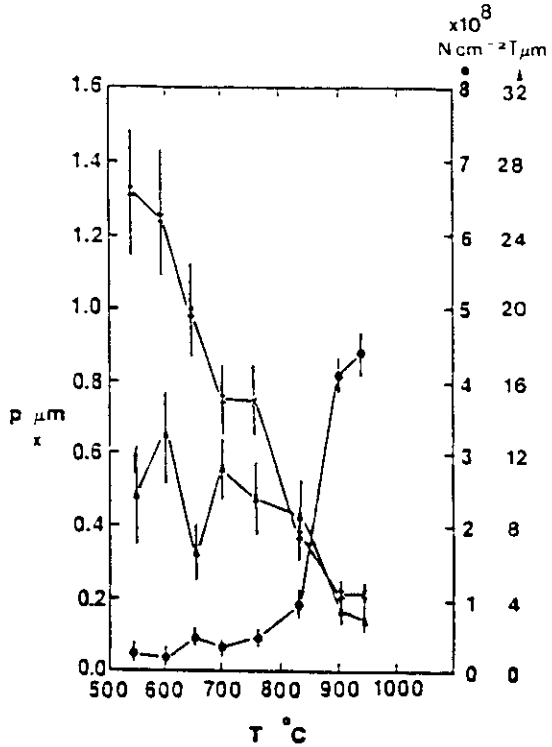

FIG. 27. Variation of average distance between dislocations, p, number density of dislocations, N, and average dislocation length, l, during thermal relaxation of a 350 Å $Ge_{0.25}Si_{0.75}$/Si(100) structure (from Hull *et al.*, 1989a).

but remains relatively constant at ~ 10 microns and actually decreases at higher temperatures. This demonstrates that dislocation nucleation plays a pivotal role in the relaxation process. The data of Fig. 27 show clearly that relaxation does not occur solely via growth of existing defects. The fact that the average dislocation length is not increasing shows also that defects are being inhibited from continual growth. Inspection of TEM images (Hull and Bean, 1989b) has indeed revealed that intersection of orthogonal dislocations frequently pins propagating defects. This "pinning probability" is strongly dependent on epilayer thickness, as is suggested by Fig. 28, which shows representative relaxation data for 350 Å and 3000 Å Ge_xSi_{1-x}/Si(100) films. It is observed that the higher thickness film is considerably more thermally unstable. Inspection of dynamic and still TEM images of the relaxation process (Hull and Bean, 1989b) has shown that this is due to the far greater ease of orthogonal dislocations crossing each other in the thicker films. This may be understood in terms of the relative misfit stress, line tension, interaction and image forces acting on the dislocations at the two different thicknesses (Hull and Bean, 1989b).

In summary, it is clear that dislocation nucleation, propagation, and interaction phenomena all play a role in determining strained-layer relaxation. The relative significance of these events in a given structure will determine its stability with respect to variations in temperature and epilayer thickness and composition.

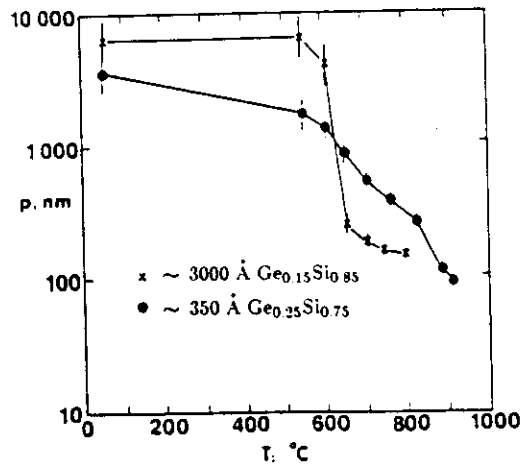

FIG. 28. Variation of average distance between misfit dislocations during thermal relaxation of (a) 350 Å $Ge_{0.25}Si_{0.75}$/Si(100) and (b) 3000 Å $Ge_{0.15}Si_{0.85}$/Si(100) (from Hull and Bean, 1989b).

E. Relaxation in Strained Clusters

It should be stressed that the two-dimensional epitaxial structures discussed so far in this section actually represent a special case in heteroepitaxial growth. In the more general case of three-dimensional or clustered growth, we should discard the concept of critical "thickness" and consider all dimensions of the strained island. The limiting case of a strained rectilinear slab has been treated theoretically by Luryi and Suhir (1986), who related the strained–dislocated transition of a slab of height h and edge length $2L$ to the configuration of a two-dimensional epilayer of thickness h via the relation

$$h_c^L = \phi(L/h)h_c^{L=\infty}. \tag{6}$$

Here h_c^L is the critical slab dimension and $h_c^{L=\infty}$ is the two-dimensional critical thickness. The reduction factor $\phi(L/h)$ is obtained from the equation

$$\phi(L/h) = \left[1 - \operatorname{sech}\left(\frac{\varepsilon L}{h\phi^2(L/h)}\right)\right]\left[1 - e^{-\pi h/L}\right]^{1/2}\left[\frac{L}{\pi h}\right]^{1/2}, \tag{7}$$

where

$$\varepsilon = \left[1.5\frac{(1-\nu)}{(1+\nu)}\right]^{1/2}.$$

These equations predict that as the slab width $2L$ decreases, the slab height at which the strained–dislocated transition occurs will increase. In fact, the Luryi–Suhir equations predict a critical edge half-length, L_c, below which the slab may be grown infinitely thick without misfit-dislocation introduction. This may be understood physically on the basis that if the slab width is less than approximately half the equilibrium average misfit-dislocation spacing for a planar structure, introduction of a single misfit dislocation into the slab–substrate interface will increase the magnitude of the lattice mismatch by making it larger but of the opposite sign to the undislocated structure.

The Luryi–Suhir model has been experimentally investigated in the GaAs–Si system (Hull and Fischer-Colbrie 1987). Cross-sectional TEM is used to probe the strain state of individual GaAs nuclei grown at 400°C on vicinal Si(100) substrates. Results are plotted in Fig. 29, which shows each island height, h, versus the ratio of island height to width (h/L). Dislocated islands are marked by crosses, whereas undislocated islands are marked by dots (note that in cross-sectional TEM, we will only observe island widths and components of dislocation Burgers vectors perpendicular to the electron beam. These experiments may thus be thought of as a two-dimensional version of the Luryi–Suhir model). A clear dependence of the undislocated–dislocated transition upon h/l is observed. Also shown are predictions of the Luryi–Suhir model. This model requires knowledge of the two-dimensional

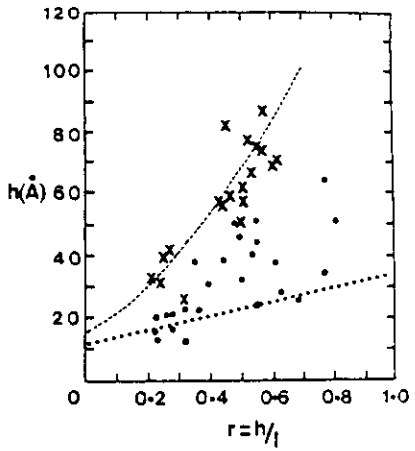

FIG. 29. Experimentally observed (via cross-sectional TEM) transitions between commensurate (●) and dislocated (×) GaAs nuclei grown on 4-degree misoriented Si(100) surfaces (from Hull and Fischer-Colbrie, 1987). The island height h is plotted on the ordinate, whereas the ratio of island height to width, (h/l) is plotted on the abscissa. The drawn curves represent the predictions of the Luryi–Suhir model using the two-dimensional critical-thickness models of People and Bean (dashed curve) and Matthews and Blakeslee (dotted line).

critical thickness as a function of varying strain in the system. Since this is not experimentally possible in the GaAs–Si system, where only one elastic mismatch is possible in the undislocated state, $h_c(\varepsilon)$ is obtained from theoretical models, namely the Matthews–Blakeslee model (1974a,b), and a more recent model by People and Bean (1985, 1986). The results of these models inputted into the Luryi–Suhir model are displayed in Fig. 29 by dotted and dashed lines, respectively. It is observed that these two theoretical curves straddle the experimental transition and are of similar form to the experimental results.

F. Critical-Thickness Phenomena in Multilayer Structures

Extension of critical-thickness concepts to multilayer structures is highly complex due to the greater degrees of freedom involved (individual layer strains and dimensions, total number of layers, total multilayer thickness, and so on). However, a simple energetic model has been developed (Hull *et al.*, 1986a) based on the reduction of the multilayer to an equivalent single strained layer.

Consider a multilayer structure consisting of n periods of the bilayers A and B, of thickness d_A and d_B and lattice-mismatch strains with respect to the substrate of ε_A and ε_B, respectively. This structure is shown schematically in Fig. 30. The total thickness, T, of the multilayer is $n(d_A + d_B)$.

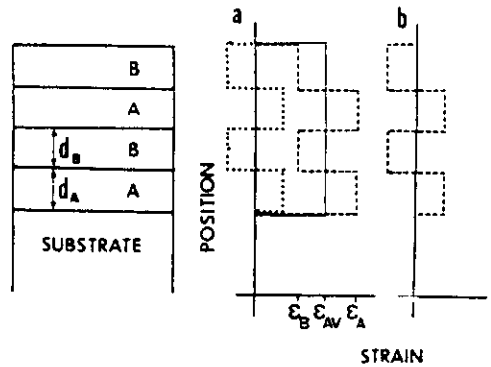

FIG. 30. Schematic illustration of criteria for structural stability of a strained-layer superlattice. (a) shows the unrelaxed superlattice and (b) its energy ground state (from Hull *et al.*, 1986a). In (a) the total strain field is shown by the dashed line and may be regarded as the supposition of a uniform strain (solid line) and an oscillating strain (dotted line).

Experimentally, it is observed that provided that each of the individual multilayers is thinner than the critical thickness for that particular layer grown directly onto the substrate (if this condition is not met, then individual interfaces within the superlattice will relax), the great majority of the strain relaxation occurs via a misfit-dislocation network at the interface between the substrate and the first strained multilayer constituent. This is demonstrated by cross-sectional TEM images of GeSi/Si and InGaAs/GaAs multilayer structures in Fig. 31. Thus, the relaxation may be regarded as occurring between the substrate and the multilayer structure as a whole.

For an undislocated structure, the elastic strain energy of the configuration in Fig. 30 would be

$$E_{un} = n(k_A d_A \varepsilon_A^2 + k_B d_B \varepsilon_B^2), \tag{8}$$

where k_A and k_B contain the relevant elastic constants for layers A and B.

Introduction of a misfit-dislocation array at the substrate–multilayer interface will change the lattice constant throughout the multilayer structure by an amount α, and the strain by an amount $\beta \sim \alpha/a_0$, where a_0 is the average bulk lattice parameter of the multilayer, such that

$$E_{dis} = n(k_A d_A(\varepsilon_A - \beta)^2 + k_B d_B(\varepsilon_B - \beta)^2). \tag{9}$$

Energy is minimized by setting $dE/d\beta = 0$, yielding

$$E_{min} = \frac{n d_A k_A d_B k_B (\varepsilon_A - \varepsilon_B)^2}{d_A k_A + d_B k_B}. \tag{10}$$

This may be regarded as the ground energy state of the superlattice with respect to dislocation formation at the substrate–multilayer interface. The

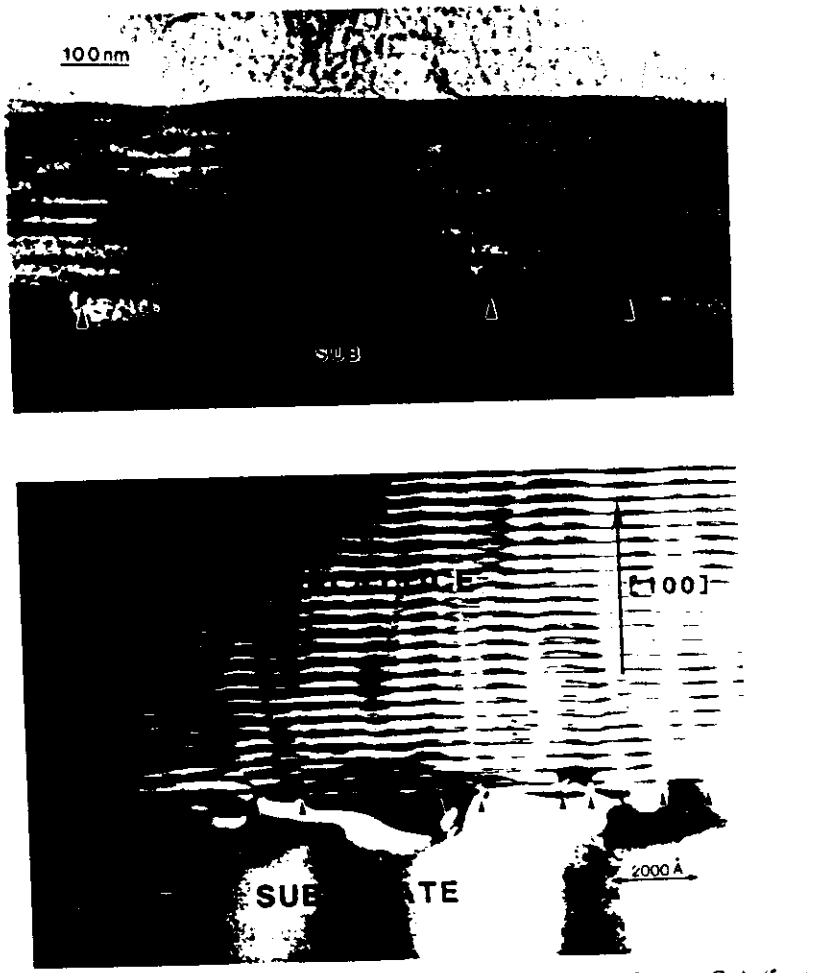

FIG. 31. Cross-sectional TEM images of (a) partially relaxed In GaAs/GaAs on GaAs (from Hull *et al.*, 1987e) and (b) GeSi/Si on Si multilayer structures (from Hull *et al.*, 1986a). Note that, as indicated by arrows, the vast majority of misfit dislocations are at the substrate–superlattice interface.

amount of energy available for relaxation by the dislocations is thus given by the energy of the undislocated state minus the energy of the ground state, (8)–(10), yielding

$$E_{rel} = \frac{n(k_A d_A \varepsilon_A + k_B d_B \varepsilon_B)^2}{d_A k_A + d_B k_B}. \qquad (11)$$

The form of this relaxable energy is equivalent to the average strain energy in the superlattice, weighted over the appropriate elastic constants and layer thicknesses. Consider a system with continuously varying strain as a function of varying composition, e.g., $In_xGa_{1-x}/GaAs$ or Ge_xSi_{1-x}/Si, where one of the superlattice constituents (say B) is the same as the substrate. If we assume that $k_A \sim k_B$ and that the elastic strain varies linearly with x, then the relaxable strain energy simplifies to that in a uniform layer of the same total thickness as the superlattice equals $n(d_A + d_B)$, and the average superlattice composition, $x_{av} = xd_A/(d_A + d_B)$. This relationship may be used as a guide for predicting the superlattice stability, based upon the experimentally determined critical thickness of single uniform strained layers of Ge_xSi_{1-x} on Si(100). In Hull *et al.* (1986a), it is shown that this model is accurate to within 20% for varying superlattice layer thicknesses of $Ge_{0.4}Si_{0.6}$ on Si(100), although as pointed out by Miles *et al.* (1988), dislocation motion through a multilayer structure is more difficult than at a single strained interface, so that at moderate temperatures, kinetic effects will limit the accuracy of the above relationship. Thus, it should be stressed that the above approach to superlattice critical thickness, while energetically correct, does not take into account atomistic details of dislocation motion and interaction. Nevertheless, it represents a reasonable first-order approximation of relating the stresses in multilayer structures to those in equivalent single layers.

G. Techniques for Dislocation Reduction in Strained-Layer Epitaxy

1. The Fundamental Problem

It is apparent that for lattice mismatches of greater than $\sim 2\%$, the critical layer thickness (of the order 100 Å from theoretical modelling and experimental measurement in different systems) becomes prohibitively small for most practical applications. For some materials combinations of high potential importance (GaAs/Si, Ge/Si, InAsSb/GaAs), the critical thickness (assuming two-dimensional growth is possible) is predicted to be ~ 10 Å. Thus, in many areas of strained-layer growth, generation of enormous quantities of interfacial misfit dislocations is unavoidable. The challenge then becomes to control the misfit-dislocation structures and distributions after they are generated.

If an epitaxial layer is of sufficient thickness, dislocations constrained at or near the interface with the substrate need not be deleterious to the materials properties of the layer sufficiently far away from the interface. Thus, electronic device fabrication in the near-surface region of a 1-micron layer need not be impeded by misfit dislocations confined to the original interface.

Unfortunately, as described earlier, a simple geometrical property of dislocations precludes the possibility that all misfit dislocations will be confined to the interface region: the need for a dislocation to terminate upon

itself, at a node with another defect, or at a free surface. A segment of interfacial misfit dislocation must then be associated with two free ends that must terminate in one of the above fashions. In general, this will mean termination at the nearest free surface, which will usually be the epilayer growth surface, because this will be at most microns from the interface, as opposed to the wafer edge, which will on average be centimeters away. Thus, each misfit-dislocation segment would be associated with two threading-dislocation ends.

The amount of strain relaxation in a lattice-mismatched system will be defined by (i) the total length of misfit dislocation and (ii) the dislocation Burgers vector. Considering the case of a constant Burgers vector, the total dislocation line length L will be given by Nl_{av}, where N and l_{av} are the number of misfit-dislocation segments and their average length, respectively. Assuming first that dislocations are noninteracting, i.e., that they must terminate at a free surface, the number of threading dislocations, N_{th}, will be given by $\sim 2N$ for $l_{av} \ll D$, the wafer diameter. We then obtain the relationship

$$N_{th} \sim \frac{2L}{l_{av}}. \tag{12}$$

Thus, as might intuitively be expected, the number of threading dislocations is inversely proportional to the average dislocation length for a given amount of strain relaxation. The ideal case, indicated schematically in Fig. 32a), is where the dislocations are essentially infinitely long, terminated only at the boundary of the wafer. The number of threading dislocations is then zero. In reality, misfit dislocations are generally of finite length (limited by dislocation nucleation, growth, and interaction rates) with $l_{av} \ll D$, as indicated schematically in Fig. 30b. High threading dislocation densities then result.

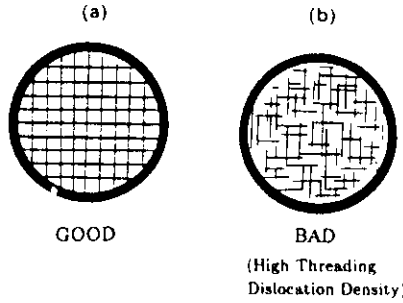

FIG. 32. Schematic illustration of the difference between (a) infinitely long misfit dislocations and (b) misfit dislocations of finite length. (from Hull *et al.*, 1989d.)

Two approaches may be adopted in reducing threading dislocation densities: (i) increase l_{av} during growth or (ii) "filter" threading dislocations after they have formed. The former possibility requires detailed knowledge of the activation barriers for dislocation nucleation and motion, as well as defect interaction mechanisms, as we have outlined in previous sections of this chapter. The latter possibility generally involves three major concepts: thermal annealing, strained-layer superlattice incorporation, and patterned growth.

2. *Effect of Thermal Annealing*

It is widely recognized (e.g., Chand *et al.*, 1986; Cho *et al.*, 1987a; Lee *et al.*, 1987) that thermal annealing either during or after the growth cycle may reduce threading-defect densities. In general, extra thermal energy will produce threading-dislocation motion, and if this process results in interaction of dislocations, defect reduction may result as indicated in Fig. 33. Interdislocation forces may either encourage or suppress defect interactions, depending upon the relative orientations of the defect Burgers vectors.

This process, although possibly producing significant improvement in material quality at relatively high defect densities (say, greater than $\sim 10^7$–$10^8\,cm^{-2}$), is unlikely to be effective at lower defect densities, $< \sim 10^6$–$10^7\,cm^{-2}$. This is because as defect densities decrease, the average spacing between threading defects necessarily increases, and this will in turn decrease the probability of defect interactions. If the original mismatched interface is fully relaxed, then the motion of the threading defects will, to a first approximation, be random during thermal annealing (local strain variations due to nonuniform defect distributions would be the major correction to this approximation), and there will be no systematic driving force for defect interactions at lower defect densities. In addition, thermal stresses arising from differential thermal expansion coefficients might act as a source for *further* defect generation in some systems.

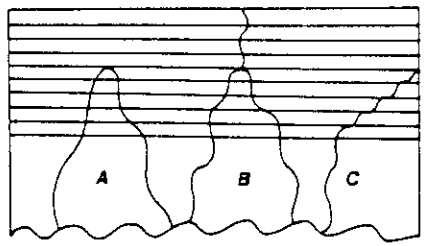

FIG. 33. Schematic illustrations of possible mechanisms for dislocation–threading arm interaction/annihilation events.

3. *"Filtering" of Threading Dislocations by Strained-Layers Superlattices*

A systematic driving force encouraging threading-defect motion in particular directions can be provided by incorporation of strained-layer superlattices into the epitaxial structure. It has long been recognized (e.g., Olsen *et al.*, 1975; Fischer *et al.*, 1986; Liliental-Weber *et al.*, 1987; Dupuis *et al.*, 1986) that strained interfaces in such superlattices may deflect threading dislocations into the interfacial planes between layers. The driving force for this process is essentially that described by the Matthews and Blakeslee mechanical equilibrium theory of lattice-mismatch relief, as outlined in an earlier section. The threading dislocations are bent into the interfacial planes to relieve mismatch at the interfaces. If care is taken with layer thicknesses, strains, and the structure growth rate, it may be possible to promote this process without generation of new mismatch-relieving dislocations.

For high threading-defect densities, this process is likely to be extremely effective at producing dislocation interactions and encouraging combination/annihilation events. For a threading-defect density $n\ \mathrm{cm}^{-2}$, the average distance between the threading dislocations will be $1/\sqrt{n}$. Thus, at threading-defect densities of $\sim 10^{10}\,\mathrm{cm}^{-2}$, typical of near-interface regions in highly lattice-mismatched systems such as GaAs/Si and Ge/Si, the average dislocation separation will be only ~ 1000 Å. Since typical dislocation velocities during growth will be of the order of microns sec^{-1} at usual growth temperatures, very little lateral deflection of threading defects will be required to produce dislocation interactions at these densities. Indeed, it was pointed out by Gourley *et al.* (1986) that even elastic moduli (with lattice parameter matching) mismatches can be sufficient to produce the necessary deflections. Thus, for very high initial defect densities, crystal quality may be expected to improve dramatically during the first few thousand Å of epilayer growth.

At moderate (for highly lattice-mismatched materials!) defect densities, however, strained-layer superlattices will be expected to become much less efficient at defect filtering. At defect densities of $10^8\,\mathrm{cm}^{-2}$, the average threading-dislocation spacing becomes 1 micron. Although, lateral motion at strained interfaces of tens or even hundreds of microns may be possible under optimum growth conditions, one has also to consider the requirement that defects interact as they laterally propagate. Since there are only four possible directions for interfacial defect propagation at (100) interfaces for $\frac{1}{2}\langle 011\rangle$ Burgers vectors dislocations moving on $\{111\}$ planes in cubic semiconductors (the 011, $0\bar{1}\bar{1}$, $01\bar{1}$, and $0\bar{1}1$ directions as shown in Fig. 34), there is a relatively narrow range of defect positions that will allow interaction. It can easily be shown geometrically (Hull *et al.*, 1989b) that the most favorable conditions for defect interaction correspond to dislocations moving towards each other on inclined $\{111\}$ glide planes with parallel intersections with the (100)

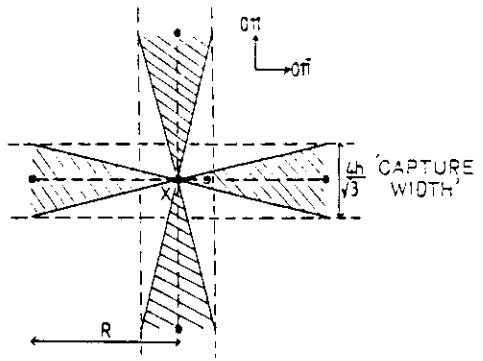

FIG. 34. Schematic diagram indicating probability of dislocation interactions (from Hull *et al.*, 1989b). The dislocation X may move in one of four [011] directions. For an average interdislocation distance R, adjacent dislocations must lie within an angle θ of these directions, where $\theta \sim 4h/R\sqrt{3}$.

interface. Under these conditions, threading-arm intersection is possible if the corresponding misfit-dislocation segments in the interfacial plane are no further apart than $2h/\sqrt{3}$, where h is the epitaxial layer thickness. This leads to the concept of a defect "capture angle," $\theta = 4h/R\sqrt{3}$, where R is the average distance between defects in the dislocation propagation direction, as illustrated in Fig. 34. Four capture angles exist, corresponding to each of the in-plane $\langle 011\rangle$ directions. Consideration of relative defect geometries and interaction probabilities in this theoretical framework (Hull *et al.*, 1989*b*) leads to the result that the average distance each dislocation has to propagate before a threading-arm intersection event is $l_{av} = \sqrt{3}/2hn$. If we assume $h = 1000$ Å, we have for $n = 10^6$, 10^8, and 10^{10}, $L \sim 1000$ microns, 10 microns, and 0.1 micron, respectively. The actual distance a threading dislocation will be expected to propagate in the interfacial plane will depend upon a number of factors including the number of strained interfaces, the layer thicknesses and lattice mismatches, the growth rate, and the growth temperature. It is apparent, however, that the probability of defect interactions decreases dramatically with decreasing threading-dislocation densities. Of the figures quoted above, a 10-micron lateral propagation seems attainable, but 1000 microns seem unlikely. This suggests that threading-dislocation filtering via strained-layer superlattices, at least by the generally assumed mechanism of defect annihilation via interaction, is likely to become ineffective at threading-defect densities of the order of 10^6–$10^8\,\mathrm{cm}^{-2}$ or below.

4. Growth on Patterned Substrates

An extremely promising technique for relaxing many of the constraints discussed previously is patterned growth onto bulk substrates. If instead of a uniform coverage of an epilayer onto a bulk substrate, selective growth (or etching) of features with dimensions much less than wafer diameter is successfully achieved, the probability of a threading defect terminating on a free edge of the structure (as opposed to the growth surface) is greatly enhanced. In the discussions above, we have ignored the possibility of threading-defect termination at the wafer edges, because in general, this would require lateral propagation of the order of centimeters (in structures that are at most microns thick). Patterned growth of structures of the order of microns or tens of microns wide will significantly relax this constraint so that annealing or strained-superlattice techniques could make these pads essentially defect free. In the ultimate extension of this technique, one could envisage pads of the order of hundreds of Å in dimension that would inhibit the *formation* of any misfit defects (Luryi and Suhir, 1986). Such pads would presently be very difficult to define by lithographic techniques, but natural seeding using porous Si substrates has been proposed (Luryi and Suhir, 1986; Lin *et al.*, 1987).

Recent work in growth of $In_xGa_{1-x}As$ on circular GaAs mesas (Fitzgerald *et al.*, 1988, 1989) has clearly shown that dramatic reductions in threading and threading-defect density may be achieved as the mesa diameter is reduced. This is believed to be both a function of reduced density of nucleation sites (reducing the number of misfit-dislocation segments) and of dislocation termination at the mesa edges, thus reducing the number of threading dislocations per misfit-dislocation segment. Representative results from this work are illustrated in Fig. 35. Recent work in epitaxial GaAs growth on patterned Si substrates has also been reported (e.g., Matyi *et al.*, 1988; Lee *et al.*, 1988).

VI. Atomic-Scale Structure of Epitaxial Layers

A. Introduction

For many devices (e.g., high-mobility modulation-doped structures and quantum-well-confined optoelectronic devices) and physical measurements (electron/hole mobilities, excitonic recombination energies, etc.), the detailed atomic atructure of epitaxial layers and their interfaces is of paramount importance. Many high-resolution experimental techniques have been developed to study this structure.

B. Theoretical Description of Isostructural Interface Structure

Perhaps the most important class of semiconductor heteroepitaxial interfaces (including almost all III-V and II-VI structures, GeSi/Si, etc.) consists of

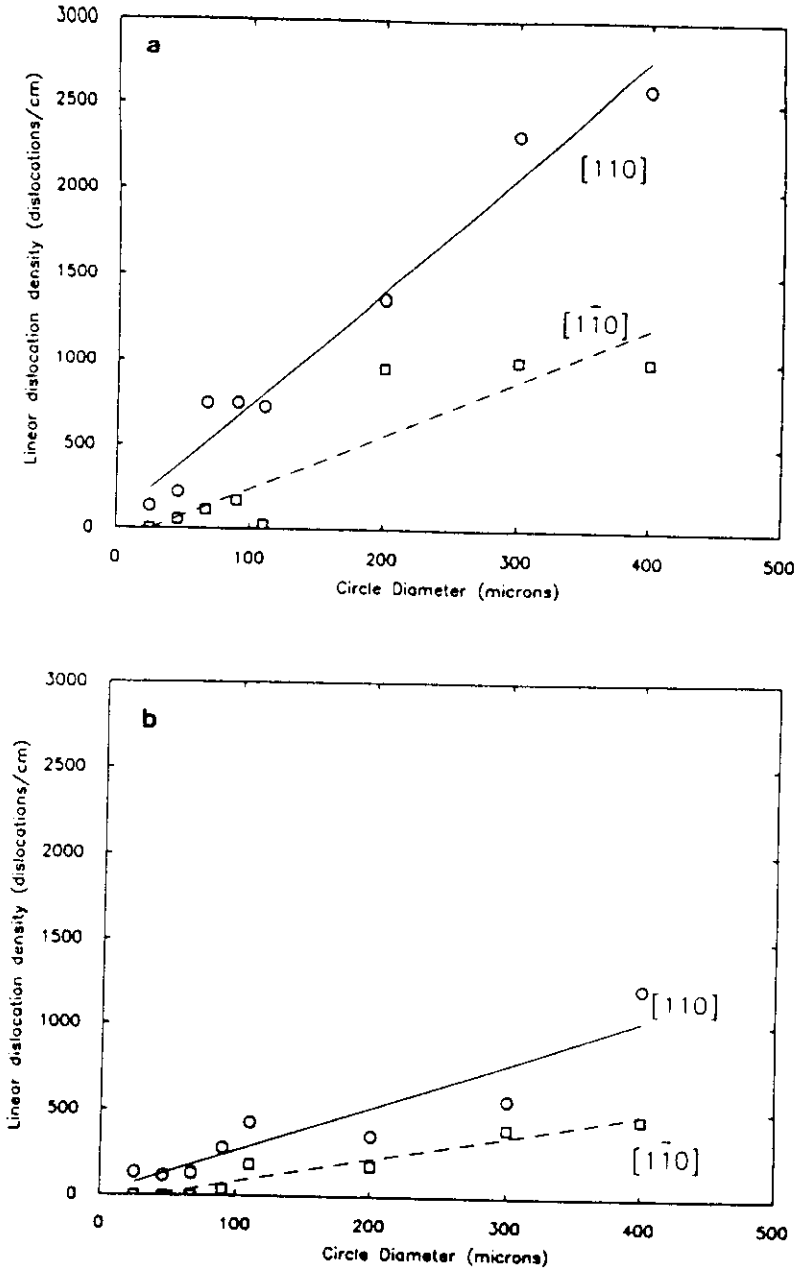

FIG. 35. Linear interface dislocation density versus circular mesa diameter for samples with 3500 Å of $In_xGa_{1-x}As$ ($x = 0.05$) grown onto GaAs with (a) $1.5 \times 10^5\,cm^{-2}$ and (b) $10^4\,cm^{-2}$ pre-existing dislocations in the substrate (from Fitzgerald *et al.*, 1989.)

isostructural interfaces, i.e., those interfaces where the crystal unit cell is of identical symmetry on either side of the interface, and the only difference is in the atomic species across the interface. Two structural parameters are generally of importance: the interface diffuseness (variation in interface structure perpendicular to the interface) and the interface roughness (variation in structure parallel to the interface). In general, an ideal interface will have zero diffuseness and roughness.

In this section, we will discuss interface roughness and diffuseness by using the model illustrated in Fig. 36 and described in more detail in Hull *et al.*, (1987d). An interface between two materials, A and B, is defined arbitrarily as lying at the boundary of 100% material A. The mean interface position is taken to be the plane $z = 0$, such that the interface lies in the x–y plane. The interface roughness is thus defined as the deviation of the interface at an arbitrary point (x_i, y_i) from the plane $z = 0$, z_i, where z_i is given by the "interface roughness function," $f(x, y)$. An interface diffuseness function, $g(z)$, then defines the perpendicular variation in composition from the interface coordinate (x_i, y_i, z_i), such that the composition at a point (x_i, y_i, z') is given by the function $g[z' - f(x_i, y_i)]$. A complete knowledge of the two functions $g(z)$ and $f(x, y)$ thus allows an exact description of the interface.

C. Origins of Interface Roughness and Diffuseness

A description of a perfect interface using the nomenclature of the previous section would be for $g(z)$ and $f(x, y)$ to be zero. Satisfaction of the condition that $f(x, y) = 0$ is essentially a thermodynamic requirement at least for oriented substrates. The primary necessity is that the growth be two-dimensional, i.e., either Frank–Van der Merwe or the earliest stages of Stranski–Krastinov, and not three-dimensional (Vollmer–Weber). Thus, as discussed in Section IV of this chapter, low growth temperatures should encourage planar heteroepitaxial interfaces. Growth of sufficiently thick layers in a system where nucleation is by the Vollmer–Weber mode may also reduce interface roughness, as individual nuclei coalesce, and further growth of that particular layer is essentially homoepitaxial, causing growth surface planarization.

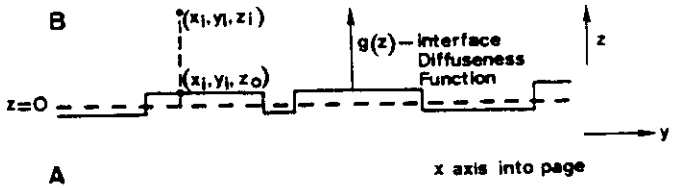

FIG. 36. Schematic illustration of the concepts of interface roughness and diffuseness, as measured by the functions $g(z)$ and $f(x, y)$, respectively (from Hull *et al.*, 1987d).

To a higher degree of perfection, for an absolutely abrupt interface, it will be necessary to grow integral numbers of monolayers, otherwise monolayer interface roughness will necessarily result. In this case, it has been shown that growth interruptions at each individual interface in compound semiconductor growth can cause significant interface smoothing (e.g., Hayakawa *et al.*, 1985; Bimberg *et al.*, 1987) by allowing surface monolayer islands to coalesce.

Interface diffuseness will generally be caused primarily by (i) source switching conditions in the growth chamber, (ii) interdiffusion of the layers at elevated growth temperatures, or (iii) interfacial exchange reactions to improve local electroneutrality (see e.g., Kroemer, 1986). Thus, for reason (ii), lower growth temperatures again encourage sharper interfaces.

The effect of source switching conditions on interface abruptness is much more difficult to ascertain. Solid sources that may be simply shuttered, as in conventional MBE, might be expected to give the sharpest interface transition. Even in this case, however, slight interface transients might be expected due to both finite speed of shutter motion and redistribution of the temperature distribution around the source as the shutter is opened and closed (this effect will be minimized if the shutter is as far away from the source as possible). In gas-source growth, such as MOCVD or GSMBE, switching conditions are generally much less ideal, and optimization of this process for a given chamber is a science in itself. Characterization of switching effects using TEM, x-ray diffraction, and photoluminescence has been attempted (e.g., Carey *et al.*, 1987; Vandenberg *et al.*, 1986).

D. Experimental Techniques

In this section, we will briefly discuss experimental techniques for determining the atomic-scale structure of interfaces. For a more complete description of experimental techniques for studying epitaxial growth in general, see Chapter 3 by S. T. Picraux *et al.* in this volume.

1. High-Resolution Transmission Electron Microscopy

Many experimental techniques have been developed to probe the structure of buried interfaces. The highest spatial-resolution (better than 2 Å) imaging technique is high-resolution transmission electron microscopy (HRTEM). Under narrowly defined experimental conditions (Spence, 1981), an HRTEM image represents a two-dimensional map of the crystal potential projected through the specimen thickness onto a plane perpendicular to the electron beam (note that, in general, HRTEM images are interpreted on the basis of numerical simulations of dynamical electron scattering, e.g., the multislice method; Goodman and Moodie, 1974). If the electron beam is aligned parallel to the interface, atomic-scale information about interface structure may be obtained subject to three major limitations: (i) Structure variations

parallel to the beam direction are averaged out. This necessitates either imaging of the same specimen area along different crystallographic zone axes (Hull *et al.*, 1986b; Batstone *et al.*, 1987) or assumptions about structural isotropy along crystallographically equivalent axes. (ii) Image noise effects tend to obscure fine image detail such as atomic steps (Gibson and McDonald, 1987). (iii) Thin-foil specimen preparation or the incident electron beam itself may modify interface structure. Despite these limitations, HRTEM has played a valuable role in elucidating interface structure in a wide variety of isostructural epitaxial systems including GeSi/Si (Hull *et al.*, 1984), GaAs/Si (Hull *et al.*, 1986*b*; Otsuka *et al.*, 1986), InGaAs/InP (Ourmazd *et al.*, 1987), AlGaAs/GaAs (Ourmazd *et al.*, 1989), and InGaAs/InAlAs (Bimberg *et al.*, 1989). Most notably, in some instances, it has been possible to correlate atomic structure with other interface or quantum confinement properties, e.g., with electronic mobilities at $Si/\alpha-SiO_2$ interfaces (Liliental *et al.*, 1985; Goodnick *et al.*, 1985) with interface state densities in CaF_2/Si (Batstone *et al.*, 1989) and photoluminescent line broadening in InAlAs/InGaAs/InAlAs quantum-well structures (Bimberg *et al.*, 1989). The experimental complications outlined earlier, however, particularly the projection and noise effects, severely limit the accuracy to which $g(z)$ and $f(x, y)$ may be determined. It has been shown (Hull *et al.*, 1987d) that detailed analysis of intensity changes across the interface as a function of interface sampling area can yield information about the magnitude of $g(z)$ and the integral of spatial frequencies of $f(x, y)$ greater than approximately the inverse of the sampling area dimensions. An example of this method is shown in Fig. 37. Line scans perpendicular to the interface in a lattice image of a $Ge_{0.4}Si_{0.6}/Si(100)$ structure are recorded with varying "slit" lengths parallel to the interface and with lattice resolution perpendicular to the interface. Many scans are recorded for each slit length. The interface "width" is plotted as a function of sampling length and approximate specimen thickness, with the product of length and thickness giving the interface area sampled. The width is defined in this case as being the number of (200) monolayers in the interface region lying within the 20%–80% intensity interval, where the 0% and 100% levels correspond to the mean intensities of the materials on either side of the interface. The plot shown in Fig. 37 demonstrates a continuously increasing interface width with sampling area. In the limit of this area tending to zero (i.e., the ordinate intersects in Fig. 37), an upper limit to the spatial extent of $g(z)$ is obtained, in this case $< \sim 2 \times (200)$ monolayers. The roughness characteristic of a particular interface area may also be continuously read from the plot, increasing to several (200) monolayers for interface sampling areas $\sim 10{,}000\ Å^2$. These values essentially correspond to the integral of the Fourier spectrum of $f(x, y)$ up to spatial frequencies comparable to the inverse of the slit length and specimen thickness. The numbers thus obtained are of physical importance in determining, for

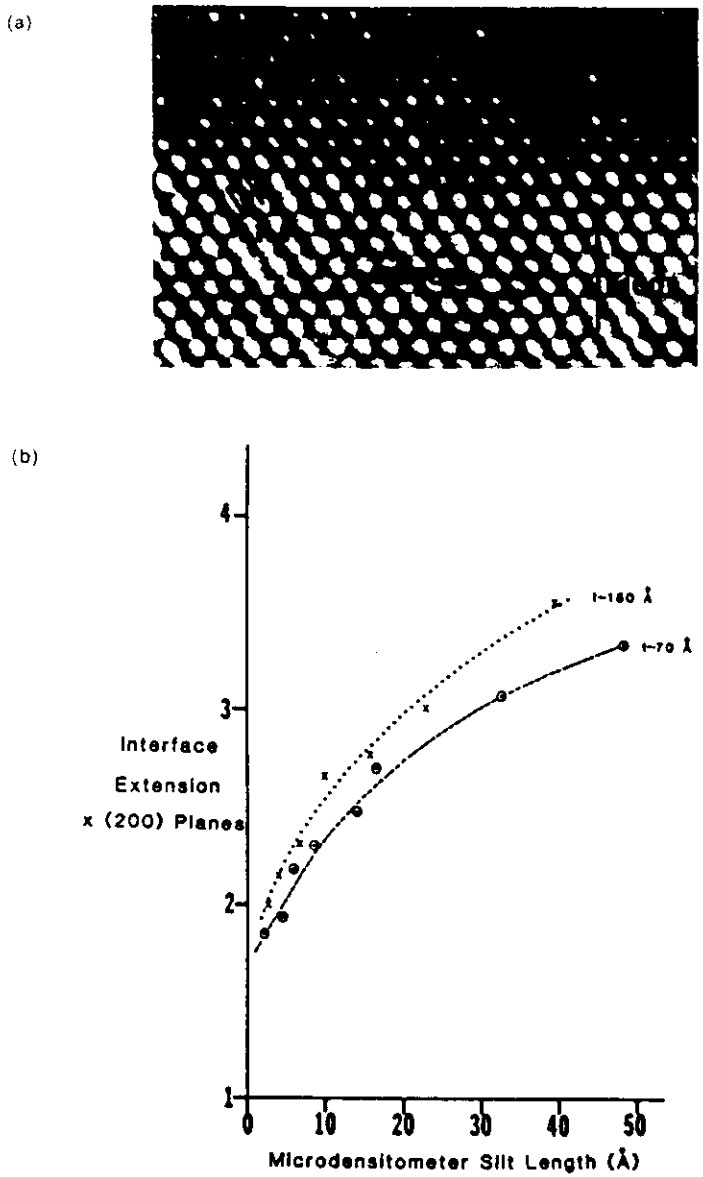

FIG. 37. (a) Cross-sectional TEM lattice structure image of a $Ge_{0.4}Si_{0.6}/Si(100)$ interface; (from Hull *et al.*, 1987d); (b) measured interface "width," w, versus slit length, L, for microdensitometer scans across the interface of the structure imaged in (a). (From Hull *et al.*, 1985. Paper originally presented at the Spring 1985 meeting of the Electrochemical Society, held in Toronto, Ontario, Canada.)

example, the characteristic interface roughness sampled within excitonic or electron wave-function diameters.

Other emerging electron microscopy techniques are proving to provide invaluable information about interface structure. Analysis of Fresnel fringe contrast at interfaces has been shown to be sensitive to interface diffuseness and is perhaps easier to interpret than lattice-structure images (Boothroyd *et al.*, 1987). Measurement of extinction-contour positional variation across interfaces in 90° wedge-shaped samples has been demonstrated to be sensitive to absolute composition variations across the interface (Kakibayashi and Nagata, 1985, 1986), and high-angle annular detection in the scanning transmission electron microscope (STEM) can give very high signal-to-noise ratio interface images (Pennycook *et al.*, 1989).

2. *Reflection High-Energy Electron Diffraction*

Perhaps the most prevalent in situ technique for determining growth-surface morphology (and thus, by inference, buried interface morphology) is RHEED. In its simplest form, it gives coarse information about surface morphology via the extent of reciprocal lattice reflections, a spotty pattern corresponding to islanded growth and a streaked pattern corresponding to two-dimensional growth (Note, however, that the observed streaks on "planar" surfaces generally arise from imperfections such as steps and terraces. For a perfectly planar surface, reciprocal lattice spots are expected—see Dobson, 1989 for a fuller discussion.) This technique, however, has recently been made dramatically more powerful and quantitative via the identification of oscillations in the RHEED intensity corresponding to completion of monolayers during two-dimensional growth (Harris *et al.*, 1981; Neave *et al.*, 1983). In principle, therefore, the smoothness of the growth surface can be determined to submonolayer precision. In addition, during a growth transition from one material to another (i.e., formation of an interface), where the amplitude of the RHEED oscillations may be expected to vary between the materials, information about the abruptness of the interface transition may, in principle, be obtained (Madhukar *et al.*, 1985).

Although RHEED is an extremely powerful and now almost routine (particularly in compound semiconductor epitaxy) growth characterization tool, some complications remain in using this technique to deduce quantitative and detailed measurements of the interface structure. By their nature, RHEED oscillations characterize growth that is close to two-dimensional, and are therefore of limited use in the more general case of three-dimensional heteronucleation. The transition from a "spotty" to a "streaked" RHEED pattern can give information about this process, but in the absence of imaging capabilities, important parameters such as nucleation density cannot be directly deduced (unless the incident beam can be spatially collimated down to dimensions comparable to individual nuclei, as can be

achieved in an electron microscope). The coherence length (approximately hundreds of Å) of the energetic electrons used in the RHEED process also naturally define a length scale on which this technique will be sensitive to surface roughness. Finally, the theory of electron scattering processes in RHEED is still at a formative stage, possibly rendering highly detailed interpretation unreliable. It should be stressed, however, that the very macroscopic nature of this technique, which lessens its impact in determining exact microscopic structure, is exactly what makes it such a powerful and crucial in situ tool for the crystal grower in determining epitaxial layer quality in real-time during growth.

Extension of the RHEED principle to imaging processes has led to the development of reflection electron microscopy (REM). For example, studies of atomic steps on clean semiconductor surfaces in ultrahigh vacuum electron microscopes have been reported (e.g., Osakabe *et al.*, 1980; Cowley, 1984).

3. *Photoluminescent Spectroscopy*

A number of authors (e.g., Deveaud *et al.*, 1984; Bimberg *et al.*, 1986; Hayakawa *et al.*, 1985; Tsang and Schubert, 1986; Ogale *et al.*, 1987, 1988) have attempted to infer interface structure from photoluminescent measurements of buried quantum wells. Clearly, the quantum confinement energy of two-dimensional excitons will be highly sensitive to exact details of the well interfacial structure. By solving the one-dimensional Schrödinger equation for the particular well shape and dimensions, it should, in principle, be possible to determine the exact excitonic recombination energy. In addition, known variations in interface structure should produce calculable excitonic energy spreads. These calculations will clearly be most sensitive for narrow well widths where quantum confinement energies are a significant proportion of the bandgap discontinuity, and monolayer variations in the well structure produce appreciable energy shifts.

If the excitonic recombination spectrum is accurately measured by using photoluminescence and photoexcitation techniques, then information about the quantum-well structure can be inferred if certain simplifying assumptions are made. For example, if it is known that the interfaces are abrupt (from RHEED or HRTEM, for example), then the energy position of the maximum of the recombination peak allows the mean well width to be calculated from a single excitonic transition, subject to certain experimental and theoretical reservations that will be discussed in the following. In addition, it should be possible to relate the shape (most simply the full width at half maximum intensity (FWHM) of the excitonic peak to the variation in well width.

Many experimental and theoretical complications arise from such interpretation, however. In the simplest case, where the interface is totally abrupt, the following factors have to considered: (i) An accurate knowledge of electron/hole effective masses (particularly in the case of high confinement

energies where the parabolic band approximation may not apply), two-dimensional excitonic binding energies, bandgaps and conduction-/valence-band discontinuities is required. Uncertainties in some of these parameters can significantly affect the accuracy of calculations at lower well widths. (ii) The material has to be low in doping and unintentional impurity levels to prevent excitonic screening effects. (iii) Other broadening effects such as band filling have to be taken into account. (iv) Barrier penetration by the wave function at low well widths becomes appreciable; thus, it is important to know the electronic properties of both the well and the barrier materials. (v) The excitonic spectrum is only sensitive to interface variations larger than a scale approximating the two-dimensional exciton diameter (itself not accurately known as a function of well width). Roughness on a scale smaller than this is "averaged out" in the spectrum.

Experimentally the simplest correlation is to measure the most intense recombination peak (i.e., the $n = 1$ to heavy-hole level) at low excitation intensities at liquid-helium temperature as a function of quantum-well width. With complementary experimental evidence regarding the interface diffuseness function, $g(z)$, this will allow the interface roughness function $f(x, y)$ to be determined for spatial periodicities greater than approximately the exciton diameter. In high-quality III-V epitaxial systems, it has been reported that single excitonic peaks can split into a doublet and triplet structure arising from monolayer interface roughness, producing relatively large regions of discrete well widths of varying sizes (Deveaud *et al.*, 1984; Hayakawa *et al.*, 1985; Bimberg *et al.*, 1986); it has also been found that interrupting growth at GaAs/AlGaAs interfaces can provide the time scale necessary for surface diffusion of growth ledges to planarize the surface and remove the doublet/triplet structures.

Further refinement of these measurements is possible by monitoring the spectrum as a function of temperature; this allows assumptions about other spectral broadening mechanisms to be validated (Bimberg *et al.*, 1986); and by varying bandgaps, it allows testing for self-consistent solutions. In systems where it is possible to simultaneously record several higher-order excitonic transitions (Tsang and Schubert, 1986), highly detailed interface interpretation may be possible, assuming theoretical modelling is sufficient. In this case, it may be possible to independently determine $g(z)$ and $f(x, y)$ from the excitonic spectrum.

As with RHEED, it should be pointed out that as a coarser tool for measuring interface quality, photoluminescent and photoexcitation techniques are powerful and convenient. In general, the recombination energy gives a relatively accurate measurement of well width, and as the width of the peak reduces, interface planarity will be increasing. More detailed conclusions, however, will require extensive experimental and theoretical interpretation.

4. *Other Experimental Techniques*

A number of other experimental tools have been developed to look either directly at the buried interface structure or indirectly via in situ monitoring of the growth surface. For example, photoemission spectroscopy has provided valuable information on the electronic structure of near-surface interfaces (e.g., Bringans *et al.*, 1985; Himpsel *et al.*, 1986; Olmstead *et al.*, 1986), ion-scattering techniques have elucidated the structure of strained metal silicide–silicon interfaces (Van Loenen, 1986), and x-Ray diffraction is particularly sensitive at determining the average structure of many interfaces in a superlattice structure (e.g., Segmuller and Blakeslee, 1973; McWhan *et al.*, 1983; Vandenberg *et al.*, 1986). Recent time-resolved low-temperature cathodoluminescence images (Bimberg *et al.*, 1987) have directly imaged monolayer high islands at GaAs/AlGaAs interfaces, and both low-energy electron diffraction (LEED) (see e.g., Henzler, 1983, for a review) and in situ electron microscopy (Gibson, 1988, 1989; Petroff, 1986; Takayanagi, 1978) have provided significant information during the growth process. Finally, Raman spectroscopy of interfacial atomic coordination in ultrafine-period (of the order of a few monolayers) structures has yielded information about interfacial planarity and diffuseness in Ge–Si multilayer structures (Tsang *et al.*, 1987; Iyer *et al.*, 1989).

E. Nonisostructural Interfaces

The above discussion has dealt primarily with isostructural interfaces, i.e., those in which the crystal structure and orientation is equivalent on either side of the interface such that the atomic positions are known but not the nature of the atomic species on each site. This turns out to be the most important class of interfaces in strained-semiconductor epitaxy because it embraces the majority of systems of technological and physical interest. A number of other interfaces are clearly of great interest, however. In some systems, the structure of the material on either side of the interface is similar or even equivalent but, generally due to a very large lattice mismatch between the materials or due to surface structure or contamination effects, the crystallographic zone axis along the growth direction is not constant across the interface. In this case, more than one orientational relationship across the interface may result. This concept is known as "double positioning" and occurs in epitaxial metal silicides on Si (Cherns *et al.*, 1984; Tung and Gibson, 1985), epitaxial fluorides on Si (Phillips *et al.*, 1988; Schowalter and Fathauer, 1986; Ishiwara *et al.*, 1985), II-VI growth on III-V surfaces (Kolodziejski *et al.*, 1986), and Al/GaAs (Liliental-Weber, 1987; Batstone *et al.*, 1987), among other systems. The easiest method of determining the orientational relationships is using diffraction techniques, particularly electron diffraction when very thin epilayers and small grain sizes are involved. In many other

nonisostructural systems, the arrangements of atoms at the interface are not self-evident (especially where the two materials have different forms of bonding), such as the epitaxial silicides and fluorides on Si discussed previously and GaAs/Si (Bringans *et al.*, 1985; Kroemer, 1986; Patel *et al.*, 1987). Arrangements of atoms at such interfaces can be studied using HRTEM (e.g., Batstone *et al.*, 1988; Cherns *et al.*, 1984; Tung and Gibson, 1985), photoemission (e.g., Bringans *et al.*, 1985; Himpsel *et al.*, 1986; Olmstead *et al.*, 1986) or x-ray diffraction (e.g., Patel *et al.*, 1987). Of these techniques, only HRTEM can analyze interface structure far away from the growth surface.

F. Structure of Epitaxial Semiconductor Alloys

1. Alloy Ordering

A great number of important epitaxial semiconductor systems, e.g., InAlAs/InGaAs, GeSi/Si, InGaAs/GaAs, InGaAs/InP, AlGaAs/GaAs, InGaAsP/InP, have one or both constituents in the form of an alloy. In the bulk form (where the bulk analogue has been studied), such alloys are generally assumed to be random structures, e.g., GeSi (Hansen, 1958). In thin-film form, it is often found that evidence for ordering of two or more of the alloy constituents exists, whether as a function of growth (kinetic) conditions or as a function of strain, such that the unit cell no longer has a random distribution of atoms within it. It is also possible that nonrandom distributions of alloy constituents may occur on a larger scale, either through clustering of like atoms, or through periodic decomposition of the alloy, such as spinodal decomposition.

The first direct evidence for long-range ordering of atoms within an epitaxial alloy unit cell was shown in the work of Kuan *et al.* (1985), who detected ordering within the unit cell of AlGaAs grown by MBE on (001) and, particularly, (110) GaAs substrates by electron diffraction, as illustrated in Fig. 38. The ordered unit-cell structure was equivalent to monolayers of AlAs and GaAs stacked along a ⟨110⟩ axis of the crystal, yielding a nominal ordered composition of $Al_{0.5}Ga_{0.5}As$. Since the work of Kuan and co-workers alloy ordering has been detected in a host of III-V ternary structures, with the ordered species lying on both the column-III and column-V sublattices (e.g., Jen *et al.*, 1986; Gomyo *et al.*, 1988; Shahid *et al.*, 1987; Ihm *et al.*, 1987). InGaAs, in particular, has been observed in several ordered states. Such semiconductor alloy ordering is analogous to ordering in metallic alloys, and virtually all ordered semiconductor states observed have their metallic analogues.

The presence of ordered domains within the alloy could strongly affect the optical and electronic properties of the material. The ordered state will have

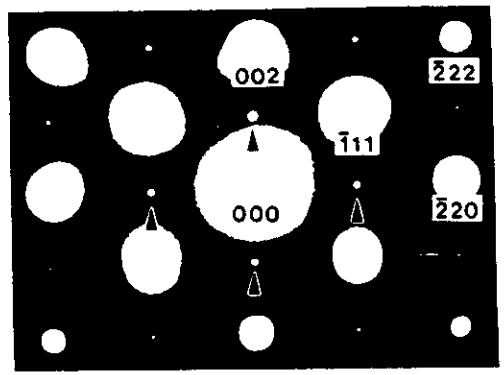

FIG. 38. Electron diffraction patterns illustrating the presence of column-III sublattice ordering in AlGaAs layers grown on GaAs. Reflections (arrowed) arise from ordering of Al and Ga atoms (from Kuan *et al.*, 1985).

different band structures (and bandgaps) from the random alloy; thus, domains of ordered material in a disordered matrix are likely to produce spectral broadening in radiative recombination processes and extra electronic scattering mechanisms. Successful growth of a perfect uniform ordered alloy, however, could be extremely desirable because it raises the prospect of a material free of disorder scattering and free of random compositional variations that might produce spectral broadening in direct bandgap alloys. Such ordered alloys would offer advantages over artificially grown monolayer or short-period superlattices that have been grown to synthesize ordered alloys (Tamargo *et al.*, 1985; Bevk *et al.*, 1986; Petroff *et al.*, 1978), since they would not be so subject to growth nonuniformities.

2. Alloy Clustering

Even if an alloy exhibits no signs of unit-cell ordering as discussed in the previous section nonrandom distributions of alloy species may still be present. The phenomenon of "clustering" of atoms of like species has been invoked (e.g., Holonyak *et al.*, 1981; Singh and Bajaj, 1984, 1985) to explain anomalously high luminescence line widths from alloys, particularly those containing Al. Consider a three-dimensional exciton of radius R in an epitaxial alloy layer of thickness $\gg R$. For a unit cell containing N_c atoms on the clustering A_xB_{1-x} sublattice and with a volume V_c, the number of A atoms within the recombining exciton volume will be

$$N_A = \frac{4\pi R^3 \times N_c}{3V_c}.$$

Gaussian statistics using the binomial approximation for large N_A would predict a variance, $\sigma_A^2 = \sqrt{N_A x(1-x)}$. The spectral broadening $\delta E/E$, where δE represents the FWHM of the spectral line then becomes $2.35(\sqrt{x(1-x)}/\sqrt{N_A}$. Using the relationships given and $E \sim 1$ eV, $V_c = (5.6)^3$ Å^3, $N_c = 8$ (for one sublattice in the zinc-blende structures), $R = 150$ Å and $x = 0.5$, one obtains δE of the order of 2 meV. This represents the lower limit to the optical line width from excitonic recombination in semiconductor alloys (Schubert *et al.*, 1984).

Experimental techniques for measurement of possible semiconductor clustering independent of optical measurements are relatively few and indirect. Experimental attempts have included those by Raman spectroscopy (Parayanthal and Pollak, 1984), infrared spectroscopy (Braunstein, 1963), and HRTEM (Hull *et al.*, 1989c). More local environments (say, first- to third-nearest neighbors) have been studied by extended x-ray absorption fine structure (Mikkelsen and Boyce, 1982) and Raman spectroscopy (Renucci *et al.*, 1971).

VII. Summary

In this chapter, we have attempted to outline present theoretical and experimental understanding of the physical processes involved in lattice-mismatched epitaxy. In this final section, we will summarize our understanding to date, emphasize those areas in which little understanding has yet emerged, and predict future directions for research.

In Section III of this chapter, we demonstrated that there can be a strong influence of the initial substrate cleaning process on subsequent hetero-epitaxial growth. This arises primarily from unexpected influences of the substrate cleaning on the resultant surface morphology. In addition, it is already well known that surface contaminants (e.g., Joyce, 1974) and surface reconstruction (e.g., Gossman, 1987) can significantly affect epitaxial growth.

Further knowledge of these processes will depend critically on development of experimental techniques to sensitively measure surface structure and contamination levels. Techniques such as LEED and RHEED give accurate information about surface reconstructions and some information about surface morphologies (terrace widths, etc.); and Auger spectroscopy can measure average surface contaminant levels to < 0.01 monolayers, but many significant effects can exist beyond the detectability level of these techniques. In situ TEM, for example (Gibson, 1989), has suggested that C contamination levels below the Auger detectability limit on a Si surface can still produce high silicon carbide particulate levels. The point here is not so much the absolute level of C contamination as its environment: a 0.01 monolayer that is evenly dispersed will be totally different from a 0.01 monolayer that has reacted to form a high density of SiC particulates. Such information is not readily available from Auger spectroscopy; and development of in situ imaging techniques such as TEM, scanning tunneling microscopy (if chemical identification can be more readily achieved), low-energy electron microscopy (Telieps, 1987), and reflection electron microscopy (see e.g., Cowley, 1984) may significantly extend our knowledge of surface processes in epitaxial growth.

The fundamentals of nucleation theory remain a much-studied topic, but the specific events that are not well understood during semiconductor epitaxial growth are interactions with surface structure and contamination, the role of nuclei coalescence boundaries in defect generation, cluster versus adatom mobility (see, e.g., Zinke-Allmang *et al.*, 1987; Venables *et al.*, 1987), and defect generation in clusters. Again, direct in situ imaging observations of these processes may help, and even nonimaging in situ techniques such as Rutherford backscattering (Zinke-Allmang *et al.*, 1987) have proven invaluable.

The primary physical process inherent to strained-layer epitaxy is that of strain relaxation via misfit-dislocation generation. Although many details of this process remain poorly understood, much progress has been made in recent years. Earlier theories of Matthews and Blakeslee for misfit-defect propagation (Matthews and Blakeslee, 1974a,b; Matthews, 1975) have been developed and extended into a general kinetic model by Dodson and Tsao (1987). Preliminary measurements of activation energies necessary to describe these kinetic processes have been reported by Hull *et al.* (e.g., 1989a), and initial attempts to describe the role of defect interactions have also been published (Dodson, 1988b; Hull and Bean, 1989b). Attempts to critically examine dislocation nucleation modes in specific systems have been made (e.g., Matthews *et al.*, 1976; Fitzgerald, 1989; Eaglesham *et al.*, 1989; Hull and Bean, 1989a; Fitzgerald *et al.*, 1989; Hagen and Strunk, 1978; Gibbings *et al.*, 1989; Dodson, 1988c), and some new candidate sources have been identified. Molecular dynamics and other computer simulations of epitaxial growth are also providing significant insight (e.g., Grabow and Gilmer, 1987; Dodson, 1984; Thomsen and Madhukar, 1987a,b,c; Choi *et al.*, 1987b). Refinement of our knowledge of these various processes should enable a complete predictive theory of strain relaxation to be developed, but much further work is required particularly in the areas of defect nucleation and interactions. Little work has been done to date on the extension of single strained-layer concepts to multilayer systems.

Experimental techniques for reducing threading-dislocation densities in thicker epitaxial layers exist, the primary tools being thermal annealing, filtering via strained-layer superlattices, and finite area growth. Of these

techniques, it appears that the first two may be useful only down to moderate defect densities, of the order of $10^6\,cm^{-2} - 10^7\,cm^{-2}$, although recent reports suggest that electric field effects may extend the useful range of strained-layer superlattice filtering to lower defect densities (Liu *et al.*, 1988; Shinohara, 1988). Techniques for patterned epitaxial growth are currently being developed with success in defect-density reduction being reported, for example, in InGaAs/GaAs (Fitzgerald *et al.*, 1988; Fitzgerald, 1989; Fitzgerald *et al.*, 1989) and GaAs/Si (Matyi *et al.*, 1988; Lee *et al.*, 1988).

Techniques for growing and measuring extremely abrupt and planar interfaces appear to be relatively advanced, as outlined in Section VI of this chapter. Molecular- and chemical-beam epitaxy techniques have advanced to the stage where interfaces that are planar and abrupt to small fractions of a monolayer may readily be synthesized (e.g., Petroff *et al.*, 1978; Tsang *et al.*, 1987; Bevk *et al.*, 1986; Bimberg *et al.*, 1986). Switching conditions in MOCVD growth, however, still appear to fall somewhat short of this. Developments of new crystal growth techniques such as ultrahigh-vacuum chemical vapor deposition (e.g., Meyerson, 1986; Meyerson *et al.*, 1988), limited reaction processing (Gibbons *et al.*, 1985, and atomic-layer epitaxy (e.g., Bedair *et al.*, 1985; Nishizawa *et al.*, 1985) may further extend epitaxial layer quality in some systems. Much fascinating science also remains to be done in understanding the exact nature of alloy materials, which are so important to many heteroepitaxial materials combinations.

In summary, much progress has been made in the last decade or so in understanding the limits of structural growth of lattice-mismatched epitaxial materials. In some systems, it is already possible to grow quasiperfect heteroepitaxial structures (misfit-defect free, with planar and abrupt interfaces), and the limits of growth of such structures are semi quantitatively known and understood. At this stage, however, it appears that in the field in general, more remains to be discovered than is already known.

Acknowledgments

We would like to acknowledge many of our colleagues who have been instrumental in their contributions to either experiments described in this chapter or our basic understanding of strained-layer epitaxy. At Bell Laboratories: D. Bahnck, J. M. Bonar, C. Buescher, N. Chand, A. Y. Cho, D. J. Eaglesham, L. C. Feldman, A. T. Fiory, G. Fitzgerald, J. M. Gibson, S. Luryi, D. M. Maher, A. Ourmazd, T. P. Pearsall, R. People, R. T. Lynch, Y. H. Xie and M. Yen; outside of Bell Laboratories: B. W. Dodson, I. J. Fritz and J. Y. Tsao (Sandia); C. M. Gronet, J. S. Harris, Jr., C. A. King, and S. M. Koch (Stanford University); K. W. Carey, A. Fischer-Colbrie, and S. J. Rosner (Hewlett Packard Laboratories); E. P. Kvam and R. Pond (University of Liverpool); P. Pirouz (Case Western University); M. Tamargo (Bell Communications Research); D. K. Biegelsen and F. A. Ponce (Xerox PARC).

References

Alexander, H., and Haasen, P. (1968). *Solid State Phys.* **22**, p. 27.

Batstone, J. L., Gibson, J. M., Tung, R. T., Levi, A. F. J., and Outten, C. A. (1987). *Mat. Res. Soc. Symp.* **82**, R. W. Siegel, J. R. Weertman, and R. Sinclair, eds. Materials Research Society, Pittsburgh, Pennsylvania, p. 335.

Batstone, J. L., Phillips, J. M., and Hunke, E. C. (1988). *Phys. Rev. Lett.* **60**, 1394.

Bauer, E., and Poppa, H. (1972). *Thin Solid Films* **12**, 167.

Bean, J. C., Feldman, L. C., Fiory, A. T., Nakahara, S., and Robinson, I. K. (1984). *J. Vac. Sci. Technol.* **A2**, 436.

Bedair, S. M., Tischler, M. A., Katsuyama, T., and Al-Masry, N. A. (1985). *Appl. Phys. Lett.* **47**, 51.

Bellevance, D. (1988). In "Silicon Molecular Beam Epitaxy," Vol. II, Ch. 13, E. Kasper and J. C. Bean, eds. CRC Press, Boca Raton, California.

Berger, P. R., Chang, K., Bhattacharya, P., Singh, J., and Bajaj, K. K. (1988). *Appl. Phys. Lett.* **53**, 684.

Bevk, J., Mannearts, J. P., Feldman, L. C., Davidson, B. A., and Ourmazd, A. (1986). *Appl. Phys. Lett.* **45**, 286.

Biegelsen, D. K., Ponce, F. A., Smith, A. J., and Tramontana, J. C. (1987). *J. Appl. Phys.* **61**, 1856.

Biegelsen, D. K., Ponce, F. A., Krusor, B. S., Tramontana, J. C., Yingling, R. D., Bringans, R. D., and Fenner, D. B. (1988). *Proc. Mat. Res. Soc.* **116**, H. K. Choi, R. Hull, H. Ishiwara, and R. J. Nemanich, eds. Materials Research Society, Pittsburgh, Pennsylvania, p. 33.

Bimberg, D., Mars, D. E., Miller, J. N., Bauer, R., and Oertel, D. (1986). *J. Vac. Sci. Technol.* **B4**, 1014.

Bimberg, D., Christen, J., Fukunaga, T., Nakashima, H., Mars, D. E., and Miller, J. N. (1987). *J. Vac. Sci. Technol.* **B5**, 1191.

Bimberg, D., Oertel, D., Hull, R., Reid, G. A., and Carey, K. W. (1989). *J. Appl. Phys.*, **65**, 2688.

Boothroyd, C. B., Britton, E. G., Ross, F. M., Baxter, C. S., Alexander, K. B., and Stobbs, W. M. (1987). *Inst. Phys. Conf. Ser.* **87**. Institute of Physics, Bristol, England, p. 195.

Braunstein, R. (1963). *Phys. Rev.* **130**, p. 879.

Bringans, R. D., Uhrberg, R. I. G., Olmstead, M. A., Bachrach, R. Z., and Northrup, J. E. (1985). *Phys. Rev. Lett.* **55**, 533.

Bruinsma, R., and Zangwill, A. (1987). *Europhys. Lett.* **4**, 729.

Carey, K. W., Hull, R., Fouquet, J. E., Kellert, F. G., and Trott, G. (1987). *Appl. Phys. Lett.* **51**, 910.

Chand, N., People, R., Baiocchi, F. A., Wecht, K. W., and Cho, A. Y. (1986). *Appl. Phys. Lett.* **49**, 815.

Chang, K. H., Berger, P. R., Gibala, R., Bhattacharya, P. K., Singh, J., Mansfield, J. F., and Clarke, R. (1988). *Proc. of TMS/AIME Symposium* on "Defects and Interfaces in Semiconductors," K. K. Rajaj, J. Narayan, and D. Ast, eds. The Metallurgical Society, Warrendale, Pennsylvania, p. 157.

Cherns, D., Hetherington, C. J. D., and Humphreys, C. J. (1984). *Phil. Mag.* **49**, 165.

Choi, C., Otsuka, N., Munns, G., Houdre, R., Morkoc, H., Zhang, S. L., Levi, D., and Klein, M. V. (1987a). *Appl. Phys. Lett.* **50**, 992.

Choi, D. K., Halicioglu, T., and Tiller, W. A. (1987b). *Proc. Mat. Res. Soc.* **94**, R. Hull, J. M. Gibson, and D. A. Smith, eds. Materials Research Society, Pittsburgh, Pennsylvania, p. 91.
Cowley, J. M. (1984). *Proc. Mat. Res. Soc.* **31**, W. Krakow, D. A. Smith, and L. W. Hobbs, eds. Materials Research Society, Pittsburgh, Pennsylvania, p. 177.
Deveaud, B., Emery, J. Y., Chomette, A., Lambert, B., and Baudet, M. (1984). *Appl. Phys. Lett.* **45**, 1078.
Dobson, P. J. (1989). *NATO ASI Series B: Physics*, Vol. 203, D. Cherns ed., Plenum Press, New York, p. 267.
Dodson, B. W. (1984). *Phys. Rev.* **B30**, 3545.
Dodson, B. W. (1988a). *Phys. Rev.* **B38**, 12383.
Dodson, B. W. (1988b). *Appl. Phys. Lett.* **53**, 37.
Dodson, B. W. (1988c). *Appl. Phys. Lett.* **53**, 394.
Dodson, B. W., and Tsao, J. Y. (1987). *Appl. Phys. Lett.* **51**, 1325.
Dupuis, R. D., Bean, J. C., Brown, J. M., Macrander, A. T., Miller, R. C., and Hopkins, L. C. (1986). *J. Elect. Mat.* **16**, 69.
Eaglesham, D. J., Kvam, E. P., Maher, D. M., Humphreys, C. J., Green, C. S., Tanner, B. K., and Bean, J. C. (1988). *Appl. Phys. Lett.* **53**, 2083.
Eaglesham, D. J., Kvam, E. P., Maher, D. M., Humphreys, C. J., and Bean, J. C. (1989). *Phil. Mag.* **A59**, 1059.
Faurie, J. P., Hsu, C., Sivananthan, S. and Chu, X. (1986a). *Surf. Sci.* **168**, 473.
Faurie, J. P., Reno, J., Sivananthan, S., Sou, I. K., Chu, X., Boukerche, M., and Wijewarnasuriya, P. S. (1988b). *J. Vac. Sci. Technol.* **B4**, 585.
Fisanick, G. J., Gossman, H.-J., and Kuo, P. (1988). *Proc. Mat. Res. Soc.* **102**, R. Tung, L. R. Dawson, and R. L. Gunshor, eds. Materials Research Society, Pittsburgh, Pennsylvania, p. 25.
Fischer, R., Masselink, W. T., Klem, J., Henderson, T., McGlinn, T. C., Klein, M. V., Morkoc, H., Mazur, J. H., and Washburn, J. (1985). *J. Appl. Phys.* **58**, 374.
Fischer, R., Morkoc, H., Neumann, D. A., Zabel, H., Choi, C., Otsuka, N., Longerbone, M., and Erickson, L. P. (1986). *J. Appl. Phys.* **60**, 1640.
Fitzgerald, E. A. (1989). *J. Vac. Sci. Tech.* **B7**, 782.
Fitzgerald, E. A., Kirchner, P. D., Proano, R. E., Pettit, G. D., Woodall, J. M., and Ast, D. G. (1988). *Appl. Phys. Lett.* **52**, 1496.
Fitzgerald, E. A., Watson, G. P., Proano, R. E., Ast, D. G., Kirchner, P. D., Pettit, G. D., and Woodall, J. M. (1989). *J. Appl. Phys.*, **65**, 2688.
Frank, F. C., and Van der Merwe, J. H. (1949a). *Proc. Roy. Soc.* **A198**, 205.
Frank, F. C., and Van der Merwe, J. H. (1949b). *Proc. Roy. Soc.* **A198**, 216.
Frank, F. C., and Van der Merwe, J. H. (1949c). *Proc. Roy. Soc.* **A200**, 125.
Fritz, I. J. (1987). *Appl. Phys. Lett.* **51**, 1080.
Fritz, I. J., Picraux, S. T., Dawson, L. R., Drummond, T. J., Laidig, W. D., and Anderson, N. G. (1985). *Appl. Phys. Lett.* **46**, 967.
Gibbings, C. J., Tuppen, C. G., and Hockley, M. (1989). *Appl. Phys. Lett.* **54**, 148.
Gibbons, J. F., Gronet, C. M., and Williams, K. E. (1985). *Appl. Phys. Lett.* **47**, 721.
Gibson, J. M. (1988). *Mat. Res. Soc. Proc.* **104**, M. Stavola, S. J. Pearton, and G. Davies, eds. Materials Research Society, Pittsburgh, Pennsylvania, p. 613.
Gibson, J. M. (1989). In "Surface and Interface Characterization by Electron Optical Methods" *NATO ASI Series B: Physics*, Vol. 191, A. Howie and U. Valdré, eds., Plenum Press, NY.
Gibson, J. M., and McDonald, M. L. (1987). In *Mat. Res. Proc. Soc.* **82**, R. W. Siegel, J. R. Weertman, and Sinclair, R. eds. Materials Research Society, Pittsburg, Pennsylvania, p. 109.
Gomyo, A., Suzuki, T., and Iijima, S. (1988). *Phys. Rev. Lett.* **60**, 2645.
Goodman, P., and Moodie, A. (1974). *Acta. Cryst. A* **30**, 280.
Goodnick, S. M., Ferry, D. K., Wilmsen, C. W., Lilliental, Z., Fathy, D., and Krivanek, O. L. (1985). *Phys. Rev.* **B32**, 8171.
Gossmann, H.-J. (1987). *Proc. Mat. Res. Soc.* **94**, R. Hull, J. M. Gibson, and D. A. Smith, eds

Materials Research Society, Pittsburgh, Pennsylvania, p. 53.
Gourley, P. L., Drummond, T. J., and Doyle, B. L. (1986). *Appl. Phys. Lett.* **49**, 1101.
Gourley, P. L., Fritz, I. J., and Dawson, L. R. (1988). *Appl. Phys. Lett.* **52**, 377.
Grabow, M., and Gilmer, G. (1987). *Proc. Mat. Res. Soc.* **94**, R. Hull, J. M. Gibson, and D. A. Smith, eds. Materials Research Society, Pittsburgh, Pennsylvania, p. 13.
Griffith, J. E., Kubby, J. A., Wierenga, P. E., and Kochanski, G. P. (1988). *Proc. Mat. Res.* **116**, H. K. Choi, R. Hull, H. Ishiwara, and R. J. Nemanich eds. Materials Research Society, Pittsburgh, Pennsylvania, p. 27.
Grunthaner, P. J., Grunthaner, F. J., Fathauer, R. W., Lin, T. L., Schowengerdt, F. D., Pate, B., and Mazur, J. H. (1988). *Proc. 2nd Int. Symp. on Si MBE*, J. C. Bean and L. J. Schowalter eds. Electrochemical Society, Pennington, New Jersey, p. 375.
Hagen, W., and Strunk, H. (1978). *Appl. Phys.* **17**, 85.
Hansen, M. (1958). In "Constitution of Binary Alloys," 2nd ed. McGraw-Hill, New York, p. 774.
Hardeman, R. W., Robbins, D. J., Gasson, D. B., and Daw, A. (1985). *Proc. 1st Int. Symp. on Si MBE*, J. C. Bean, ed. Electrochemical Society, Pennington, New Jersey, p. 16.
Harris, J. J., Joyce, B. A., and Dobson, P. J. (1981). *Surf. Sci.* **103**, L90.
Harris, J. S., Jr., Koch, S. M., and Rosner, S. J. (1987). In "Heteroepitaxy on Si II," *Proc. Mat. Res. Soc.* **91**, J. C. C. Fan, J. M. Phillips, and B.-Y. Tsaur eds. Materials Research Society, Pittsburg, Pennsylvania, p. 3.
Hayakawa, T., Suyama, T., Takahashi, K., Kondo, M., Yamamoto, S., Yano, S., and Hijikata, T. (1985). *Appl. Phys. Lett.* **47**, 952.
Henderson, R. C. (1972). *J. Electrochem. Soc.* **119**, 772.
Henzler, M. (1983). *Surf. Sci.* **132**, 82.
Himpsel, F. J., Karlsson, U. O., Morar, J. F., Rieger, D., and Yarmoff, J. A. (1986). *Phys. Rev. Lett.* **56**, 1497.
Hirsch, P. B., Howie, A., Nicholson, R. B., Pashley, D. W., and Whelan, M. J. (1977). "Electron Microscopy of Thin Crystals," 2nd ed. Robert E. Krieger, Malabar, Florida.
Hirth, J. P., and Lothe, J. (1968). "Theory of Dislocations." McGraw-Hill, New York.
Holonyak, N., Jr., Laidig, W. D., Camras, M. D., Morkoc, H., Drummond, T. J., Hess, K., and Burroughs, M. S. (1981). *J. Appl. Phys.* **52**, 7201.
Hull, R., and Bean, J. C. (1989). *J. Vac. Sci. Technol.* **A7**, 2580.
Hull, R., and Bean, J. C. (1989b). *Appl. Phys. Lett.* **54**, 925.
Hull, R., and Fischer-Colbrie, A. (1987). *Appl. Phys. Lett.* **50**, 851.
Hull, R., Gibson, J. M., and Bean, J. C. (1984). *Appl. Phys. Lett.* **46**, 179.
Hull, R., Bean, J. C., Fiory, A. T., Gibson, J. M., and Hartsough, N. E. (1985). *Proc. 1st Int. Symp. on Si MBE*, J. C. Bean, S. S. Iyer, E. Kasper, and Y. Shiraki, eds., Electrochemical Society, Pennington, NJ, p. 376.
Hull, R., Bean, J. C., Cerdeira, F., Fiory, A. T., and Gibson, J. M. (1986a). *Appl. Phys. Lett.* **48**, 56.
Hull, R., Rosner, S. J., Koch, S. M., and Harris, J. S., Jr. (1986b). *Appl. Phys. Lett.* **49**, 1714.
Hull, R., Fischer-Colbrie, A., Rosner, S. J., Koch, S. M., and Harris, J. S., Jr. (1987a). *Appl. Phys. Lett.* **51**, 1723.
Hull, R., Fischer-Colbrie, A., Rosner, S. J., Koch, S. M., Harris, J. S., Jr. (1987b). *Proc. Mat. Res. Soc.* **94**, R. Hull, J. M. Gibson, and D. A. Smith, eds. Materials Society, Pittsburgh, Pennsylvania, p. 23.
Hull, R., Bean, J. C., Leibenguth, R. E., Koch, S. M., and Harris, J. S., Jr. (1987c). *Proc. 2nd Int. Symp. on Si MBE*, J. C. Bean and L. J. Schowalter, eds. Electrochemical Society, Pennington, New Jersey, p. 293.
Hull, R., Reid, G. A., and Carey, K. W. (1987d). *Proc. Mat. Res. Soc.* **77**, J. D. Dow, I. K. Schuller, and J. Hilliard, eds. Materials Research Society, Pittsburgh, Pennsylvania, p. 261.
Hull, R., Turner, J. E., Fischer-Colbrie, A., White, A. E., Short, K. T., Pearton, S. J., and Tu, C. W. (1987e). *Proc. Mat. Res. Soc.* **93**, U. Gibson, A. E. White, and P. P. Pronko, eds. Materials Research Society, Pittsburgh, Pennsylvania, p. 153.
Hull, R., Yen, M. Y., Werder, D. J., Short, K. T., and Cho, A. Y. (1988a). Unpublished work.

Hull, R., Bean, J. C., Werder, D. J., and Leibenguth, R. E. (1988b). *Appl. Phys. Lett.* **52**, 1605.
Hull, R., Bean, J. C., Koch, S. M., and Harris, J. S., Jr. (1988c). In "Dislocations and Interfaces in Semiconductors," K. Rajan, J. Narayan, and D. G. Ast, eds. The Metallurgical Society, Warrendale, PA, p. 77.
Hull, R., Bean, J. C., Werder, D. J., and Leibenguth, R. E. (1989a). *Phys. Rev. B.* **40**, 1681.
Hull, R., Bean, J. C., Leibenguth, R. E., and Werder, D. J. (1989b). *J. Appl. Phys.* **65**, 4723.
Hull, R., Flores, J. R., and Bean, J. C. (1989c). Unpublished.
Hull, R., Bean, J. C., Bahek, D., Bonar, J. M., and Buescher, C. (1989d). *NATO ASI Series B: Physics*, Vol. 203, D. Cherns, ed., Plenum Press, New York, p. 381.
Hull, R., Bean, J. C., Eaglesham, D. J., Bonar, J. M., and Buescher, C. (1989e). *Thin Solids Films* **183**, 117.
Ihm, Y. E., Otsuka, N., Klem, J., and Morkoc, H. (1987). *Appl. Phys. Lett.* **51**, 2013.
Ishiwara, H., Asano, T., and Kanemura, S. (1985). *Proc. 1st Int. Symp. on Si MBE*, J. C. Bean, S. S. Iyer, E. Kasper, and Y. Shiraki, eds. Electrochemical Society, Pennington, New Jersey, p. 285, and references therein.
Ishizaka, A., Nakagawa, K., and Shiraki, Y. (1983). *Proc. of the 2nd Int. Conf. on Molecular Beam Epitaxy and Related Clean Surface Techniques*. Japan Society of Applied Physics, Tokyo, p. 183.
Iyer, S. S., Tsang, J. C., Copel, M. W., Pukite, P. R., and Tromp, R. M. (1989). *Appl. Phys. Lett.* **54**, 219.
Jen, H. R., Cherng, M. J., and Stringfellow, G. B. (1986). *Appl. Phys. Lett.* **48**, 1603.
Joyce, B. A. (1974). *Rep. Prog. Phys.* **37**, 363.
Kakibayashi, H., and Nagata, F. (1985). *Japan J. Appl. Phys.* **24**, L905.
Kakibayashi, H., and Nagata, F. (1986). *Japan J. Appl. Phys.* **25**, 1644.
Kaplan, R. (1980). *Surf. Sci.* **93**, 145.
Kasper, E., Herzog, H.-J., and Kibbel, H. (1975). *Appl. Phys.* **8**, 199.
Koch, S. M., Rosner, S. J., Hull, R., Yoffe, G. W., and Harris, J. S. Jr., (1987). *J. Crystal Growth* **81**, 205.
Kolodziejski, L. A., Gunshor, R. L., Otsuka, N., and Choi, C. (1986). *J. Vac. Sci. Technol.* **A4**, 2150.
Kroemer, H. (1986). *Proc. Mat. Res. Soc.* **67**, J. C. C. Fan and J. M. Poate, eds. Materials Research Society, Pittsburgh, Pennsylvania, p. 3.
Kuan, T. S., Kuech, T. F., Wang, W. I., and Wilkie, E. L. (1985). *Phys. Rev. Lett.* **54**, 201.
Kvam, E. P., Eaglesham, D. J., Maher, D. M., Humphreys, C. J., Bean, J. C., Green, G. S., and Tanner, B. K. (1988). *Proc. Mat. Res. Soc.* **104**, M. Stavola, S. J. Pearton, and G. Davies, eds. Materials Research, Pittsburg, Pennsylvania, p. 623.
Lee, H. P., Huang, Y-H., Liu, X., Lin, H., Smith, J. S., Weber, E. R., Yu, P., Wang, S., and Lilliental-Weber, Z. (1988). *Proc. Mat. Res. Soc.* **116**, H. K. Choi, R. Hull, H. Ishiwara, and R. J. Nemanich, eds. Materials Research Society, Pittsburgh, Pennsylvania, p. 219.
Lee, J. W., Shichijo, H., Tsai, J. L., and Matyi, R. J. (1987). *Appl. Phys. Lett.* **50**, 31.
Lewis, B. F., Grunthaner, F. J., Madhukar, A., Lee, T. C., and Fernandez R. (1985). *J. Vac. Sci. Technol.* **B3**, 1317.
Liliental-Weber, Z. (1987). *J. Vac. Sci. Technol.* **B5**, 1007.
Liliental, Z., Krivanek, O. L., Goodnick, S. M., and Wilmsen, C. W. (1985). *Mat. Res. Proc.* **37**, J. M. Gibson and L. R. Dawson, eds. Materials Research Society, Pittsburgh, Pennsylvania, p. 193.
Liliental-Weber, Z., Weber, J., Washburn, J., Liu, T. Y., and Kroemer, H. (1987). *Proc. Mat. Res. Soc.* **91**, J. C. C. Fan, J. M. Phillips, and B.-Y. Tsaur, eds. Materials Research Society, Pittsburgh, Pensylvania, p. 91.
Lin, T. L., Sadwick, L., Wang, K. L., Kao, Y. C., Hull, R., Nieh, C. W., Jamieson, D. N., and Liu, J. K. (1987). *Appl. Phys. Lett.* **51**, 814.
Liu, T. Y., Petroff, P. M., and Kroemer, H. (1988). *J. Appl. Phys.* **52**, 543.
Luryi, S., and Suhir, E. (1988). *Appl. Phys. Lett.* **49**, 140.

Madhukar, A., Lee, T. C., Yen, M. Y., Chen, P., Kim, J. Y., Ghaisas, S. V., and Newman, P. G. (1985). *Appl. Phys. Lett.* **46**, 1148.
Matteson, S., and Bowling, R. A. (1988). *J. Vac. Sci. Technol.* **B6**, 2504.
Matthews, J. W. (1975). *J. Vac. Sci. Technol.* **12**, 126, and references therein.
Matthews, J. W., and Blakeslee, A. E. (1974a). *J. Crystal Growth* **27**, 118.
Matthews, J. W., and Blakeslee, A. E. (1974b). *J. Crystal Growth* **32**, 265.
Matthews, J. W., Blakeslee, A. E., and Mader, S. (1976). *Thin Solid Films* **33**, 253.
Matyi, R. J., Shichijo, H., and Tsai, H. L. (1988). *J. Vac. Sci. Technol.* **B6**, 699.
McWhan, D. B., Gurvitch, M., Rowell, J. M., and Walker, L. R. (1983). *J. Appl. Phys.* **54**, 3886.
Meyerson, B. S. (1986). *Appl. Phys. Lett.* **48**, 797.
Meyerson, B. S., Uram, K. J., and LeGoues, F. K. (1988). *Appl. Phys. Lett.* **53**, 2555.
Mikkelsen, J. C., and Boyce, J. B. (1982). *Phys. Rev. Lett.* **49**, 1412.
Miles, R. H., McGill, T. C., Chow, P. P., Johnson, D. C., Hauenstein, R. J., Nieh, C. W., and Strathman, M. D. (1988). *Appl. Phys. Lett.* **52**, 916.
Mott, N. F., and Nabarro, F. R. N. (1940). *Proc. Phys. Soc.* **52**, 86.
Nabarro, F. R. N. (1940). *Proc. Roy. Soc.* **A175**, 519.
Nabarro, F. R. N. (1967). "Theory of Crystal Dislocations." Clarendon Press, Oxford, England.
Neave, J. H., Joyce, B. A., Dobson, P. J., and Norton, N. (1983). *Appl. Phys.* **A31**, 1.
Nishi, S., Inomata, H., Akiyama, M., and Kaminishi, K. (1985). *Japan J. Appl. Phys.* **24**, L391.
Nishizawa, J., Abe, H., and Kurabayashi, T. (1985). *J. Electrochem. Soc.* **132**, 197.
Ogale, S. B., Madhukar, A., Voillot, F., Thomsen, M., Tang, W. C., Lee, T. C., Kim, J. Y., and Chen, P. (1987). *Phys. Rev.* **B36**, 1662.
Ogale, S. B., Madhukar, A., and Cho, N. M. (1988). *J. Appl. Phys.* **63**, 578.
Ohno, E. R., and Williams, E. D. (1989). *Jap. J. Appl. Phys.* **28**, L2061.
Olmstead, M. A., Uhrberg, R. I. G., Bringans, R. D., and Bachrach, R. Z. (1986). *J. Vac. Sci. Technol.* **B4**, 1123.
Olsen, G. H., Abrahams, M. S., Buiocchi, G. J., and Zamerowski, T. J. (1975). *J. Appl. Phys.* **46**, 1643.
Osakabe, N., Tanashiro, Y., Yagi, K., and Honjo, G. (1989). *Surf. Sci.* **97**, 393.
Otsuka, N., Choi, C., Nakamura, Y., Nagakuva, S., Fischer, R. F., Peng, C. K., and Morkoc, H. (1986). *Proc. Mat. Res. Soc.* **67**, J. C. C. Fan and J. M. Poate, eds. Materials Research Society, Pittsburgh, Pennsylvania, p. 85.
Ourmazd, A., Tsang, W. T., Rentschler, J. A., and Taylor, D. W. (1987). *Appl. Phys. Lett.* **50**, 1417.
Ourmazd, A., Taylor, D. W., Cunningham, J., and Tu, C. W. (1989). *Phys. Rev. Lett.* **62**, 933.
Parayanthal, P., and Pollak, F. H. (1984). *Phys. Rev. Lett.* **52**, 1822.
Parker, E. H. C., and Whall, T. E. (1988). *Proc. 2nd Int. Symp. on Si MBE*, J. C. Bean and L. J. Schowalter, eds. The Electrochemical Society, Pennington, New Jersey, p. 347.
Patel, J. R., and Chaudhuri A. R. (1966). *Phys. Rev.* **143**, 601.
Patel, J. R., Freeland, P. E., Hybertsen, M. S., Jacobson, D. C., and Golvechenko, J. A. (1987). *Phys. Rev. Lett.* **59**, 2180.
Peierls, R. E. (1940). *Proc. Phys. Soc.* **52**, 23.
People, R., and Bean, J. C. (1985). *Appl. Phys. Lett.* **47**, 322.
People, R., and Bean, J. C. (1986). *Appl. Phys. Lett.* **49**, 229.
Pennycook, S. J., Jesson, D. E., and Chisholm, M. J. (1989). *Inst. Phys. Conf. Ser. 100*, Institute of Physics, Bristol, England, p. 195.
Petroff, P. M., Gossard, A. C., Wiegmann, W., and Savage, A. (1978). *J. Crystal Growth* **44**, 5.
Petroff, P. M. (1986). *J. Vac. Sci. Technol.* **B4**, 874.
Phillips, J. M., Batstone, J. L., and Hensel, J. C. (1988). *Proc. Mat. Res. Soc.* **116**, H. K. Choi, R. Hull, H. Ishiwara, and R. J. Nemanich, eds. Materials Research Society, Pittsburgh, Pennsylvania, p. 403, and references therein.
Pirouz, P., Ernst, F., and Cheng, T. T. (1988). *Proc. Mat. Res. Soc.* **116**, H. K. Choi, R. Hull, H. Ishiwara, and R. J. Nemanich, eds. Materials Research Society, Pittsburgh, Pennsylvania, p. 57.

Ponce, F. A., Anderson, G. B., and Ballingal, J. M. (1967). *Proc. Mat. Res. Soc.* **90**, R. F. C. Farrow, J. F. Schetzina, and J. T. Cheung, eds. Materials Research Society, Pittsburgh, Pennsylvania, p. 199.
Rajan, K., and Denhoff, M. (1987). *J. Appl. Phys.* **62**, 1710.
Reno, J. L., Gourley, P. L., Monfroy, G., and Faurie, J. P. (1988). *Appl. Phys. Lett.* **53**, 1747.
Renucci, M. A., Renucci, J. B., and Cardona, M. (1971). In "Light Scattering in Solids." M. Balkanski, ed., Flammarion, Paris, France, p. 326.
Rubloff, G. W., Tromp, R. M., van Loenen, E. J., Balk, P., and LeGoues, F. (1986). *J. Vac. Sci. Technol.* **A4**, 1024.
Sakamoto, T., Funabashi, H., Ohta, K., Nakagawa, T., Kawai, N. J., Kojima, T., and Bando, Y. (1985). *Superlattices and Microstructure* **1**, 347.
Schowalter, L. J., and Fathauer, R. W. (1986). *J. Vac. Sci. Technol.* **A4**, 1026, and references therein.
Schubert, E. F., Gobel, E. O., Horikoshi, J., Ploog, K., and Queisser, H. J. (1984). *Phys. Rev.* **B30**, 813.
Segmuller, A., and Blakeslee, A. E. (1973). *J. Appl. Cryst.* **6**, 19.
Shahid, M. A., Mahajan, S., and Laughlin, D. E. (1987). *Phys. Rev. Lett.* **58**, 2567.
Shinohara, M. (1988). *Appl. Phys. Lett.* **52**, 543.
Singh, J., and Bajaj, K. K. (1984). *Appl. Phys. Lett.* **44**, 1075.
Singh, J., and Bajaj, K. K. (1985). *J. Appl. Phys.* **57**, 5444.
Spence, J. C. H., (1981). "Experimental High Resolution Electron Microscopy." Clarendon Press, Oxford.
Stranski, I. N., and Krastanow, L. (1939). *Akad. Wiss. Mainz L. Math.-Nat.* KIIIb **146**, 797.
Tabe, M. (1984). *Appl. Phys. Lett.* **45**, 1073.
Tabe, M., Arai, K., and Nakamura, H. (1981). *Japan J. Appl. Phys.* **20**, 703.
Takayanagi, K., Yagi, K., Kobayashi, K., and Honjo, G. (1978). *J. Phys.* **E11**, 441.
Tamargo, M. C., Hull, R., Greene, L. H., Hayes, J. R., and Cho, A. Y. (1985). *Appl. Phys. Lett.* **46**, 569.
Telieps, W. (1987). *Appl. Phys.* **A44**, 55.
Thomsen, M., and Madhukar, A. (1987a). *J. Crystal Growth* **80**, 275.
Thomsen, M., and Madhukar, A. (1987b). *J. Crystal Growth* **84**, 79.
Thomsen, M., and Madhukar, A. (1987c). *J. Crystal Growth* **84**, 98.
Tromp, R. M., Rubloff, G. W., Balk, P., LeGoues, F., and van Loenen, E. J. (1985). *Phys. Rev. Lett.* **55**, 2322.
Tsang, J. C., Iyer, S. S., and Delage, S. L. (1987). *Appl. Phys. Lett.* **51**, 1732.
Tsao, J. Y., Dodson, B. W., Picraux, S. T., and Cornelison, D. M. (1987). *Phys. Rev. Lett.* **59**, 2455.
Tsang, W. T. and Schubert, E. F. (1986). *Appl. Phys. Lett.* **49**, 220.
Tung, R. T., and Gibson, J. M. (1985). *J. Vac. Sci. Technol.* **A3**, 987.
Vandenberg, J. M., Chu, S. N. G., Hamm, R. A., Panish, M. B., and Temkin, H. (1986). *Appl. Phys. Lett.* **49**, 1302.
Van der Merwe, J. H., and Ball, C. A. B. (1975). In Epitaxial Growth," Part B, J. W. Matthews, ed. Academic Press, New York, pp. 193–528.
Van Loenen, E. J. (1986). *J. Vac. Sci. Technol.* **A4**, 939.
Venables, J. A., Doust, T., and Kariotis, R. (1987). *Proc. Mat. Res. Soc.* **94**, R. Hull, J. M. Gibson, and D. A. Smith, eds. Materials Research Society, Pittsburgh, Pennsylvania, p. 3, for a general review of nucleation theory.
Wierenga, P. E., Kubby, J. A., and Griffith, J. E. (1987). *Phys. Rev. Lett.* **59**, 2169.
Xie, Y.-H, Wu, Y. Y., and Wang, K. L. (1986). *Appl. Phys. Lett.* **48**, 287.
Yen, M. Y., Levine, B. F., Bethea, C. G., Choi, K. K., and Cho, A. Y. (1987). *Appl. Phys. Lett.* **50**, 927.
Zinke-Allmang, M., Feldman, L. C., and Nakahara, S. (1987). *Appl. Phys. Lett.* **51**, 975.